RESEARCH ARTICLE

Key Points:
- Unprecedented aerosol hygroscopicity and refractive index data across North America up to several kilometers
- Narrow range of RI (real portion only) values (1.52–1.54) seen for all air mass classifications
- Modeling the evaporation of semivolatile species during aerosol particle measurements

Supporting Information:
- Supporting Information S1

Correspondence to:
A. Sorooshian,
armin@email.arizona.edu

Airborne characterization of subsaturated aerosol hygroscopicity and dry refractive index from the surface to 6.5 km during the SEAC⁴RS campaign

Taylor Shingler[1], Ewan Crosbie[2,3], Amber Ortega[1], Manabu Shiraiwa[4], Andreas Zuend[5], Andreas Beyersdorf[2], Luke Ziemba[2], Bruce Anderson[2], Lee Thornhill[2,6], Anne E. Perring[7,8], Joshua P. Schwarz[7], Pedro Campazano-Jost[8,9], Douglas A. Day[8,9], Jose L. Jimenez[8,9], Johnathan W. Hair[2], Tomas Mikoviny[10], Armin Wisthaler[10,11], and Armin Sorooshian[1,12]

[1]Department of Chemical and Environmental Engineering, University of Arizona, Tucson, Arizona, USA, [2]Langley Research Center Chemistry and Dynamics Branch, National Aeronautics and Space Administration, Hampton, Virginia, USA, [3]Oak Ridge Associated Universities, Oak Ridge, Tennessee, USA, [4]Multiphase Chemistry Department, Max Planck Institute for Chemistry, Mainz, Germany, [5]Department of Atmospheric and Oceanic Sciences, McGill University, Montreal, Quebec, Canada, [6]Science Systems and Applications, Inc., Hampton, Virginia, USA, [7]Chemical Sciences Division, Earth System Research Laboratory, National Oceanic and Atmospheric Administration, Boulder, Colorado, USA, [8]Cooperative Institute for Research in Environmental Sciences, University of Colorado Boulder, Boulder, Colorado, USA, [9]Department of Chemistry and Biochemistry, University of Colorado Boulder, Boulder, Colorado, USA, [10]Department of Chemistry, University of Oslo, Oslo, Norway, [11]Institute for Ion Physics and Applied Physics, University of Innsbruck, Innsbruck, Austria, [12]Department of Atmospheric Sciences, University of Arizona, Tucson, Arizona, USA

Abstract In situ aerosol particle measurements were conducted during 21 NASA DC-8 flights in the Studies of Emissions and Atmospheric Composition, Clouds, and Climate Coupling by Regional Surveys field campaign over the United States, Canada, Pacific Ocean, and Gulf of Mexico. For the first time, this study reports rapid, size-resolved hygroscopic growth and real refractive index (RI at 532 nm) data between the surface and upper troposphere in a variety of air masses including wildfires, agricultural fires, biogenic, marine, and urban outflow. The Differential Aerosol Sizing and Hygroscopicity Spectrometer Probe (DASH-SP) quantified size-resolved diameter growth factors ($GF = D_{p,\text{wet}}/D_{p,\text{dry}}$) that are used to infer the hygroscopicity parameter κ. Thermokinetic simulations were conducted to estimate the impact of partial particle volatilization within the DASH-SP across a range of sampling conditions. Analyses of GF and RI data as a function of air mass origin, dry size, and altitude are reported, in addition to κ values for the inorganic and organic fractions of aerosol. Average RI values are found to be fairly constant (1.52–1.54) for all air mass categories. An algorithm is used to compare size-resolved DASH-SP GF with bulk scattering $f(\text{RH} = 80\%)$ data obtained from a pair of nephelometers, and the results show that the two can only be reconciled if GF is assumed to decrease with increasing dry size above 400 nm (i.e., beyond the upper bound of DASH-SP measurements). Individual case studies illustrate variations of hygroscopicity as a function of dry size, environmental conditions, altitude, and composition.

1. Introduction

As aerosol particles are exposed to changing relative humidity (RH), some undergo a change in their size owing to hygroscopic growth (via water uptake) or shrinkage (via evaporation) with the magnitude of this change dependent on their chemical composition. The extent to which aerosol particles change size affects the radiation budget as larger particles scatter more light and increase the planetary albedo. Particles of higher hygroscopicity grow to larger sizes (at fixed RH) and have greater cloud condensation nuclei (CCN) activity, influencing cloud microphysical properties and the hydrologic cycle. Aerosol hygroscopicity also has significant effects on air quality, visibility, and public health. Despite decades of research devoted to aerosol-water interactions, their treatment is either lacking in models or characterized by uncertain parameterizations [e.g., *Lohmann and Feichter*, 2005; *Levin and Cotton*, 2009; *Betancourt and Nenes*, 2014]. Consequently, these interactions are among the largest sources of uncertainty in current estimates of the total anthropogenic radiative forcing budget [*Intergovernmental Panel on Climate Change*, 2013]. This is due, in part, to limitations of current observational tools and the complexity of physicochemical processes, short lifetime, and spatial inhomogeneity of aerosol particles.

Improved knowledge of aerosol hygroscopicity is needed for remote sensing applications, especially those involving aerosol optical depth from satellite-borne sensors such as Aqua/Terra Moderate Resolution Imaging Spectroradiometer and the Multiangle Imaging Spectroradiometer. The application of satellite data to investigations of aerosol-cloud interactions, which often rely on a proxy for aerosol number concentration [e.g., *Kaufman et al.*, 2005; *Myhre et al.*, 2007], involves a conversion from columnar measurements of extinction to aerosol number. This calculation requires assumptions about the aerosol size distribution and scattering cross section. Often, the assumed size distribution is based on in situ measurements of dried aerosol while the remote measurements are necessarily made under ambient conditions. This can lead to overestimations of aerosol number from satellite measurements, especially in the vicinity of clouds. To further probe aerosol-cloud interactions and link surface measurements with satellite data, it would be beneficial to increase our understanding of how to treat aerosol hygroscopicity with both size and vertically resolved measurements.

The need to quantify the subsaturated hygroscopic properties of ambient aerosols has led to a number of instrument designs over past decades, including recently the Differential Aerosol Sizing and Hygroscopicity Probe (DASH-SP, Brechtel Mfg. Inc.) [*Sorooshian et al.*, 2008a]. The DASH-SP was specifically designed to carry out rapid (approximately seconds) size-resolved ($D_{p,dry}$ between 180 and 400 nm) measurements of subsaturated particle hygroscopicity on airborne platforms. The other commonly used instrument is the Humidifed Tandem Differential Mobility Analyzer (HTDMA) [*Liu et al.*, 1978; *Rader and McMurry*, 1986], which typically requires several minutes to measure the size distribution of humidified particles using a DMA. Such low time resolution is not ideal for airborne measurements, especially when encountering narrow plumes or conducting aircraft ascents and descents to examine vertical variability. Both the HTDMA and DASH-SP quantify size-resolved hygroscopic growth factors (GF = $D_{p,wet}/D_{p,dry}$), which is the ratio of the sphere-equivalent particle diameter at an elevated RH (typically, a value between 70 and 95%) compared to that for dry conditions (typically <20% RH). Another category of instruments, nephelometers, examine the ratio, termed f(RH), of total light scattered between a humidified channel (typically ~80% RH) and a dried channel (typically ~20% RH). Relative to the DASH-SP, nephelometers also have rapid time resolution but include a number of limitations [*Kreidenweis and Asa-Awuku*, 2014]: (i) different dry size distributions with identical composition can yield different f(RH) values due to the nonlinearity of light scattering as a function of particle size, as described by Mie theory; (ii) RHs are typically kept below 85% to prevent internal condensation; and (iii) intercomparisons between different f(RH) measurements are difficult due to the variability in laser wavelength and dry RH values used.

The overwhelming majority of measurement studies focused on subsaturated hygroscopicity have been surface-based [e.g., *Swietlicki et al.*, 2008, and references therein]. Of the few reported airborne measurements of size-resolved GF, they have been greatly limited in temporal and spatial (horizontal and vertical) resolution, with most restricted to the lowest few kilometers of the troposphere [e.g., *Hegg et al.*, 2006; *Sorooshian et al.*, 2008b; *Hersey et al.*, 2013; *Rosati et al.*, 2015]. Measurements off the California coast suggest that GF increases from an altitude 30 m to 250 m in the marine boundary layer possibly due to oxidation of organic films [*Hegg et al.*, 2006]. A different study in that region, in the same altitude range, showed that GF decreased between below-cloud to above-cloud regions owing to a higher organic volume fraction in the free troposphere above cloud [*Hersey et al.*, 2009]. *Rosati et al.* [2015] used a white-light humidified optical particle spectrometer to collect vertical GF profiles between 100 and 700 m in Po Valley, Italy, and showed that early morning values in GF are reduced later in the day when a less hygroscopic aerosol layer aloft mixes with the lower layer. Previous studies with the DASH-SP have also focused on specific sources such as a large cargo ship [*Murphy et al.*, 2009], a large cattle feedlot [*Sorooshian et al.*, 2008b], and Los Angeles [*Hersey et al.*, 2013] without much focus on vertical features but instead on horizontal variations within a fairly narrow spatial range.

As measurement studies such as those described above often examine hygroscopicity at different RHs, it is convenient to report hygroscopicity results as a RH-independent value by using a single parameter that can be used in models such as kappa (κ [*Petters and Kreidenweis*, 2007]) used in the κ-Köhler theory of hygroscopic growth. GF data collected by the aforementioned instruments at any RH, in addition to CCN measurements in the regime supersaturated with respect to liquid water saturation, can be related to a value of κ. In the subsaturated regime, κ is directly related to GF using the approximation shown in

equation (1) (where RH corresponds to the mole fraction-based water activity in a liquid particle phase in equilibrium with the gas phase).

$$[GF]^3 = 1 + \kappa \left(\frac{\frac{RH}{100\%}}{1 - \frac{RH}{100\%}} \right) \tag{1}$$

f(RH) data are frequently used to estimate κ values by first inferring a GF value from the f(RH) measurement using size distribution information and Mie theory [*Zieger et al.*, 2010; *Cappa et al.*, 2011]. As large inventories of f(RH) data already exist [*Kreidenweis and Asa-Awuku*, 2014, and references therein] and continue to be collected, it is of interest to examine how best to relate f(RH) to model parameterizations of hygroscopicity. Having a data set with concurrent size-resolved GF and bulk f(RH) measurements allows for a direct comparison between hygroscopicity measurements to determine if a single calculated GF value can be applied to all particle sizes in a distribution to determine values for single parameter representations of hygroscopicity.

Aside from the GF measurement, the DASH-SP instrument can measure the real component of the refractive index (RI) for dry particles at a wavelength of 532 nm. RI values as a function of wavelength are used to constrain the radiative forcing of ambient particles, as well as to aid in the use and interpretation of remote sensing data [e.g., *Toon et al.*, 1976; *Dubovik and King*, 2000; *Dubovik et al.*, 2000; *Redemann et al.*, 2000; *Dubovik et al.*, 2002] and atmospheric models [e.g., *Kaufman et al.*, 1997; *Chin et al.*, 2002]. The real part of RI is associated with light scattering, whereas the imaginary part is linked to absorption. A wide range of RI values (real part) have been reported in the literature (usually between 1.4 and 1.6) with the differences reported to be due to factors such as wavelength examined, dry particle size, air mass types, and composition [e.g., *Westphal and Toon*, 1991; *Ferrare et al.*, 1998; *Yamasoe et al.*, 1998; *Sokolik and Toon*, 1999; *Hand and Kreidenweis*, 2002; *Guyon et al.*, 2003; *Raut and Chazette*, 2008; *Sorooshian et al.*, 2008b; *Wex et al.*, 2009; *Kim and Paulson*, 2013; *Ferrero et al.*, 2014; *Rosati et al.*, 2015]. Many models obtain optical property data from look-up tables in the Global Aerosol Data Set, which lists species categories having refractive indices with a real component between ~1.50 and 1.53 at 532 nm, with the exception of soot and sulfuric acid droplets [*Koepke et al.*, 1997]. Building a larger data inventory of vertically resolved RI in diverse air masses will benefit calculations of aerosol radiative forcing, as well as validation and use of remote sensing data of aerosol optical properties.

The goal of this study is to report on airborne subsaturated particle hygroscopicity and dry particle RI measurements collected during the Studies of Emissions and Atmospheric Composition, Clouds, and Climate Coupling by Regional Surveys (SEAC⁴RS) campaign between August and September of 2013 over the continental United States, Canada, the Pacific Ocean, and the Gulf of Mexico. The deployment of the DASH-SP on the NASA DC-8 aircraft represents the first time rapid subsaturated size-resolved GF and dry particle RI measurements have been conducted from the surface to the upper troposphere. Furthermore, the DC-8 aircraft consisted of a payload with a rich set of complementary data that are crucial to the interpretation of DASH-SP results, including f(RH), aerosol particle composition, and gas-phase composition. This study reports on the following: (i) updated techniques in the use of DASH-SP data including modeling of potential sampling bias due to evaporation of semivolatile species in the instrument; (ii) a statistical summary of subsaturated, size-resolved GF and RI (at 532 nm) data and compositing of the data as a function of instrument sampling RH, particle dry size ($D_{p,\text{dry}}$), and air mass type; (iii) intercomparison of the DASH-SP data with the more commonly used nephelometer f(RH) measurement of bulk aerosol hygroscopicity; and (iv) selected case study analyses and vertically resolved data findings.

2. Instruments and Methods

2.1. SEAC⁴RS Campaign

The DASH-SP was deployed on the NASA DC-8 during the SEAC⁴RS field campaign, which included three aircraft and was based in Houston, Texas. DASH-SP data were reported from all 21 research flights (map in Figure 1) including two transit flights between Palmdale, California, and Houston, Texas. The DC-8 flew over a range of altitudes from near the surface up to over 12 km above sea level (asl). Aerosol measurements with the DASH-SP and other instruments discussed in this study were conducted concurrently using the same dry aerosol inlet from the University of Hawaii shrouded solid diffuser inlet [*McNaughton et al.*, 2007], which operated isokinetically.
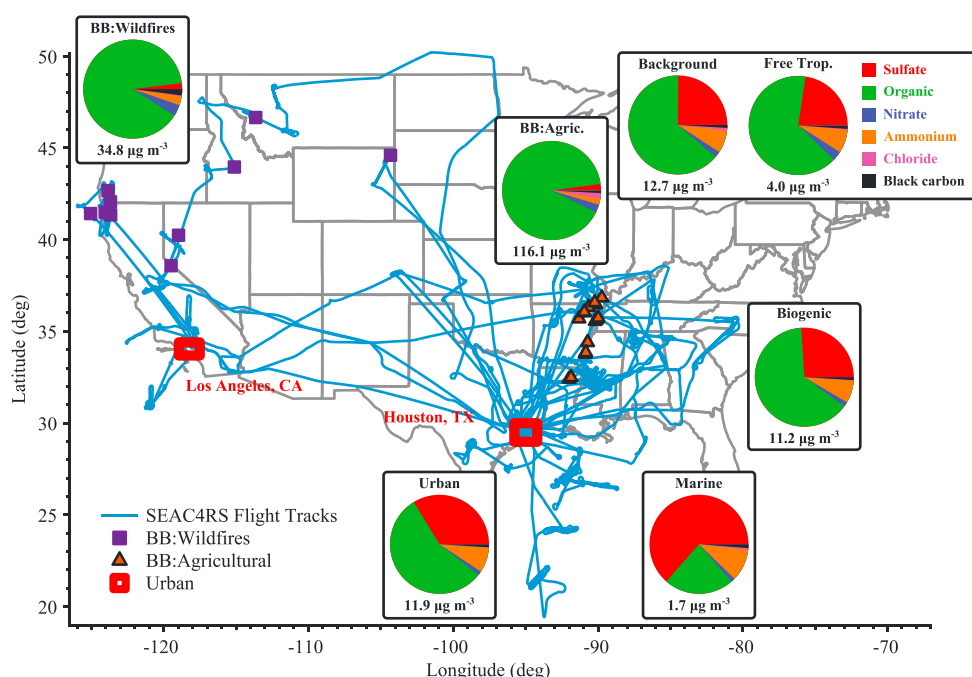
Figure 1. Map of all 23 (21 research, 2 test) flight tracks during SEAC⁴RS. PM_1 composition (mass fractions) and average total aerosol mass are shown for each air mass classification as determined by HR-AMS and HD-SP2. The urban area air mass classification is designated as measurements retrieved within the planetary boundary layer (PBL) of the two urban areas highlighted in red. Locations of the wildfires (squares) and agricultural fires (triangles) sampled are indicated at the point of peak CO concentration during a particular plume transect.

2.2. Differential Aerosol Sizing and Hygroscopicity Spectrometer Probe

The DASH-SP, illustrated in Figure 2, couples a single classification DMA system with two parallel channels consisting of controlled humidification and sizing modules. The modules that comprise the instrument are, in the order in which the aerosol experiences them: (1) an aerosol dryer, (2) an aerosol charge neutralizer, (3) a classification DMA that selects the dry mobility size range for which growth factor measurements are made, (4) a diffusion-based aerosol conditioning module in which particles are brought to equilibrium at a controlled RH, and detectors at the outlet end that either determine (5a) the optical scattering distribution of dry, monodisperse particles selected by the DMA (used to determine the real component of RI at 532 nm), or (5b) the optical scattering distribution of the particles after the RH conditioning module. The optical particle counters (OPCs) measuring the light scattering rely on diode lasers at a wavelength of 532 nm (World Star Technologies, Model TECGL-30), with details about the light collection provided elsewhere [*Sorooshian et al.*, 2008a]. The sample residence time between the instrument inlet and the entrance to the humidifier is approximately 3 s, whereas the sample residence time through the humidifier and optical particle counters (OPCs) is approximately 4 s. Previous work by *Sjogren et al.* [2007] has indicated that a residence time of 4 s may not be sufficient to reach full equilibrium during hydration of some solid organic particles, potentially underestimating growth by up to 7%. Hydration equilibration times inside the DASH-SP are explored further in section 3. During the SEAC⁴RS campaign, the DASH-SP instrument sampled particles with dry diameters between 180 and 400 nm, with the humidified channel RH varying between 40 and 95% but with most data collected at RHs between 70 and 95%.

The DASH-SP deployed in SEAC⁴RS is a modified form of the prototype DASH-SP, which has been extensively characterized with laboratory tests by *Sorooshian et al.* [2008a] and deployed successfully in previous aircraft [*Sorooshian et al.*, 2008b; *Hersey et al.*, 2009, 2013] and surface-based campaigns [*Hersey et al.*, 2011]. The key differences include a new and faster humidification system in place of a nafion-based system, which made it possible to replace three humidified channels with one, thereby reducing size, weight, and power demands. A key advantage of the custom-built diffusion humidifier is that no physical barrier exists between the humidifying airflow and the sample flow to be humidified. Therefore, the technique does not suffer from the large
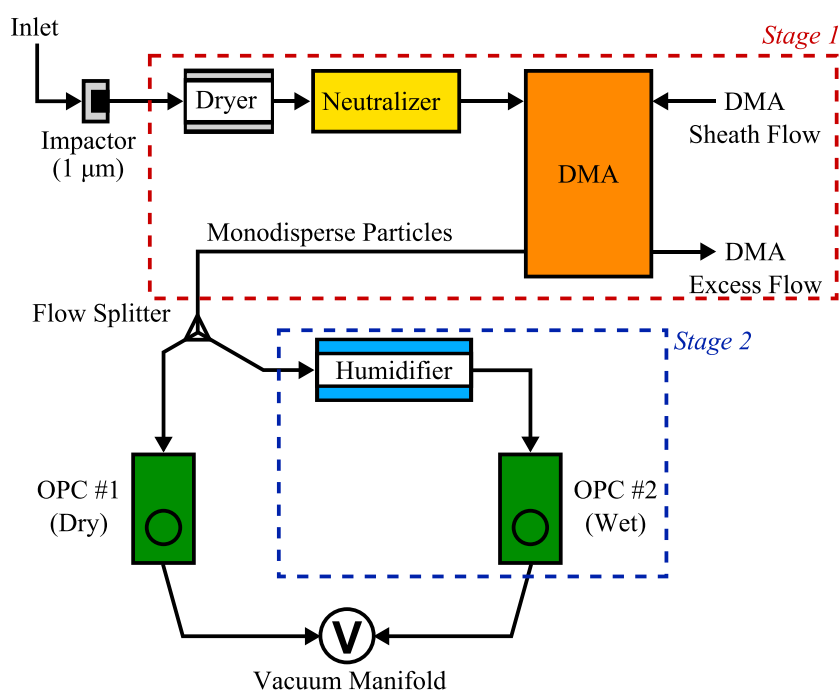
Figure 2. Schematic of the DASH-SP instrument, summarizing the transport path of sampled aerosol particles. Flow stages for semivolatile species losses, described in section 3, are indicated by the dashed boxes. (DMA = differential mobility analyzer, OPC = optical particle counter, V = vacuum pump).

hysteresis effects seen in nafion-based systems and exhibits a much faster time response, significantly reducing the time required to equilibrate between RH changes.

As compared to previous DASH-SP studies, an updated approach has been developed to process the raw data to improve peak detection in lower signal-to-noise ratio scans and to allow multiple means to be retained for each distribution. Briefly, the optical scattering populations are registered by the instrument as electrical pulse height distributions and are analyzed using a penalized least squares approach (Tikhonov regularization) to simplify the complex distribution of particle optical sizes identified by the DASH-SP to just two average values representative of the entire population. This allows multiple means to be retained for each distribution. The process is set to iterate the fit until only two means remain, as typically there is either (i) one dominant primary signal plus a much smaller doubly charged population, or, less frequently, (ii) a significant bimodal distribution in one or both channels. The data processing code identifies these two means and selects the dominant of the two to then be used in the iterative data processing algorithm that has been used in previous DASH-SP studies and described by *Sorooshian et al.* [2008a]. That original algorithm is used to quantify dry particle refractive index (RI_{dry}) and GF. The RI_{dry} is calculated from a calibration surface using the dry OPC response and the known dry particle diameter, selected by the DMA. The $D_{p,dry}$ and RI_{dry} are used as initial conditions in an iterative data processing algorithm with another calibration surface to determine the volume-weighted RI_{wet} and $D_{p,wet}$. The two calibration surfaces are created using salts with a range of known refractive indices (i.e., LiF, Na_2SO_4, K_2SO_4, $(NH_4)_2SO_4$, NaCl, and polystyrene latex spheres) at 36 dry mobility size settings between 150 and 500 nm. Calibrations were conducted before, during, and after SEAC^{4}RS. The algorithm assumes that particles are spherical. However, during calibrations, the cubic nature of NaCl is accounted for by using a dynamic shape factor of 1.08 [*Hameri et al.*, 2001; *Zelenyuk et al.*, 2006].

Strict quality control filters were applied to omit data when critical instrument parameters (temperature, pressure, RH, and flow rates) exceeded a tolerable threshold level of variability. RH is typically controlled to within 1.5%, and overall uncertainty in GF calculations is less than 3%. Wet salt tests were frequently conducted on the ground to check that the humidified RH values reported by the instrument agreed with documented deliquescence RH values for salts such as $(NH_4)_2SO_4$, Na_2SO_4, and NaCl. It is noted that particles with an appreciable imaginary component of the complex refractive index, as is the case with black and brown carbon, have the

ability to impact the OPC scattering signal [*Sorooshian et al.*, 2008a; *Forrister et al.*, 2015]. However, the black carbon component is a very small fraction of the overall particle composition of particles sampled during SEAC⁴RS (as explained later in section 4.1) and absorption would likely have a very small impact on the OPC measurements. This is further supported by single scattering albedo (SSA) results reported in section 4.1.

Due to additional complexities of operating on an airborne platform, additional quality control steps are implemented to retain a high level of data accuracy. Scans without a sufficient number of particles counted in the OPCs within a minute (<100 particles per distribution) were discarded. The majority of scans have particle counts that are conserved between the channels. Scans with significantly different counts between the channels are typically situations where (i) the sample flow rates are slightly off from the set point, in which count discrepancies between channels can be corrected for using flow rate data, or (ii) the sampled particles have grown out of the detection window when sampling at the upper limit of dry sizes. In the latter situation, these scans were omitted. When sampling aerosol particles in clouds, larger water droplets can impact the aerosol inlet and shatter into small particles leading to sampling artifacts in aerosol instruments. To avoid this issue, all analyses were limited to data collected outside of clouds.

2.3. Other Instrumentation

The analysis of DASH-SP data is greatly enhanced by the inclusion of numerous other data sets on the DC-8 relevant to aerosol physicochemical properties, gas-phase composition, and meteorological data, which were all time-synchronized. Data used from the Langley Aerosol Research Group (LARGE) instrument package include f(RH) derived from tandem humidified nephelometers (TSI Inc, St. Paul, MN, USA; Model 3563) [*Ziemba et al.*, 2013] and number size distributions from the Laser Aerosol Spectrometer (LAS; D_p between 0.1 and 6.3 μm), derived using a RI_{dry} value of 1.60. In this analysis, modal D_p values were determined as the size bin from the number size distribution with the maximum number of counts. The f(RH) measurement was conducted at a humidified and dry RH of 80% and 20%, respectively.

Gas-phase data for selected species (e.g., acetonitrile, isoprene, monoterpenes, methyl-vinyl-ketone, and methacrolein) used in classifying different air mass sources were obtained from a Proton-Transfer-Reaction Mass Spectrometer (PTR-MS) [*de Gouw and Warneke*, 2007]. Submicron, nonrefractory aerosol composition was measured by the Aerodyne High-Resolution Time-of-Flight Aerosol Mass Spectrometer (HR-AMS) [*DeCarlo et al.*, 2006; *Canagaratna et al.*, 2007]. Elemental ratios reported for the organic fraction use the recently improved calibration described in *Canagaratna et al.* [2015]. Black carbon (BC) mass concentrations were obtained using the Humidified-Dual Single-Particle Soot Photometer (HD-SP2) [*Schwarz et al.*, 2015]. Submicron species mass fractions were calculated using the sum of species from the HR-AMS (total organic, sulfate, nitrate, ammonium, and chloride) and HD-SP2 (BC). Water vapor data are used from the Diode Laser Hygrometer [*Diskin et al.*, 2002]. Carbon monoxide data are used from the folded-path, differential absorption mid-IR diode laser spectrometer [*Sachse et al.*, 1987]. A High Spectral Resolution Lidar (HSRL) [*Hair et al.*, 2008] retrieved vertical profiles of aerosol backscattering and extinction at 532 nm. All data are publicly available from the NASA Langley Research Center Atmospheric Science Data Center [*Atmospheric Science Data Center*, 2015].

2.4. Air Mass Classifications

To determine the dominant emission source contributing to the composition of a sampled air mass, a classification system was used to distinguish between the following seven sources: (i) biomass burning from wildfires (BB-Wildfires), (ii) biomass burning from agricultural fires (BB-Agricultural), (iii) biogenic, (iv) marine, (v) urban, (vi) background, and (vii) free troposphere (FT). For categories that are intended to include only data in the mixing layer (i.e., marine, urban, and background), it was necessary to define the top of the planetary boundary layer (PBL), which is considered here as the altitude above the surface with the highest rate of change in water vapor concentration during vertical profiles.

The gas-phase species acetonitrile has been used to identify air masses influenced by biomass burning products [*de Gouw et al.*, 2004]. For this study, air masses have been classified as biomass burning by periods when acetonitrile exceeded 250 parts per trillion by volume (pptv) (significantly greater than background levels) or carbon monoxide (used when acetonitrile data were unavailable) exceeded 250 ppbv. Biomass burning data were further differentiated between wildfires and agricultural prescribed crop burns based on size, origin, and visual observation during flights. Locations of individual fires sampled during SEAC⁴RS are designated in Figure 1. To reduce the number of false positive biomass burning signals, the carbon monoxide flag was removed over urban areas highlighted in Figure 1.

Biogenic sources have previously been identified by elevated levels of the dominant biogenic volatile organic compound (BVOC) species [e.g., *Weber et al.*, 2007] such as isoprene, monoterpenes, methyl-vinyl ketone, and methacrolein. In this study, an air mass is classified as having a biogenic chemical signature if the concentration sum of the four aforementioned BVOC species exceeded 2 ppbv, with acetonitrile concentrations less than 250 pptv. A second biogenic classification (monoterpenes greater than 200 pptv, acetonitrile less than 250 pptv) was used to identify purely coniferous forest emissions. However, the results for both biogenic criteria were extremely similar, and thus, only the total sum classification was chosen for simplicity, which may slightly bias the classification toward more isoprene-rich sources.

Marine air mass sources were limited to PBL measurements conducted over the Gulf of Mexico or Pacific Ocean, greater than ~40 km from the coast. The urban air mass type was identified as being within the PBL and geographically located above either of the two major urban centers sampled during SEAC⁴RS, including Houston, Texas (bounded by 30.50°N, −94.60°W to 29.00°N, −96.10°W) and Los Angeles, California (bounded by 34.17°N, −117.00°W to 33.44°N , −119.75°W). For data not falling into any of the first five categories, they were classified as either background or FT depending on whether they were in or above the PBL, respectively. Data that qualified as fitting into more than one of the first five categories are termed here as "mixed" and are not a major focus of this study.

3. Modeling of Semivolatile Species Losses

Proper accounting of semivolatile organic compounds (SVOCs) in aerosol physicochemical measurements is important as they may have a measureable impact on water-uptake properties. It is expected that as aerosol are drawn in from ambient conditions outside the aircraft, the change in temperature (due to ram heating upon entering the inlet and heat transfer to both the inlet and instrument within the cabin, as well as deliberate heating/cooling in the instrument) and mixing with filtered sheath flow air (lacking SVOCs in the vapor phase), leads to evaporation of SVOCs and semivolatile inorganic compounds from the particle phase. This evaporation ultimately impacts the chemical composition and hygroscopic growth characteristics of the aerosol particles.

Thermo-kinetic modeling of evaporative losses of semivolatile species in the DASH-SP sampling lines was conducted using selected organic and inorganic species representing classes of atmospherically relevant components of different volatilities and chemical structures. The predicted evaporation behavior presented here is specific for the conditions of the DASH-SP instrument and could be applicable to other such instruments possessing the range of conditions (residence time, dilution with particle-free air, and temperature changes) simulated. Some instruments, such as the HR-AMS, have an order-of-magnitude lower sampling residence time and do not dilute the sampling line, and thus, evaporation in their inlets will play a much smaller role than estimated here. The Aerosol Inorganic-Organic Mixtures Functional groups Activity Coefficients [*Zuend et al.*, 2008, 2011] thermodynamic model was used to determine species activity coefficients and the number of condensed phases of mixed organic-inorganic aerosol particles at gas-particle and liquid-liquid equilibrium conditions for a given system both at initial ambient conditions and at instrument temperature using established computational methods [*Zuend et al.*, 2010; *Zuend and Seinfeld*, 2013]. The kinetic multilayer model for gas-particle interactions in aerosols and clouds [*Shiraiwa et al.*, 2012, 2013] was used to model the transient re-equilibration processes experienced by aerosol particles as they change temperature and vapor-phase concentrations inside the instrument during sampling. The sampling line was split into two stages illustrated in Figure 2: drying ("Stage 1") and humidifying ("Stage 2"). The drying portion of the instrument includes the dryer (assumed to reach 10% RH), DMA, and monodisperse sampling lines up to the humidifier, having a combined residence time of 3 s. The humidifying stage starts at the inlet to the diffusion-based humidifier and ends at the OPC exit, having a residence time of 4 s. All modeling parameters are listed in Table 1. We note that the AMS inlet residence time was ~0.3 s, and thus, evaporated fractions should be significantly smaller for the composition measurements.

Ammonium nitrate, a common aerosol-phase semivolatile compound (present as NH_3 and HNO_3 in the gas phase), and two subsets of SVOC species were selected (Table 2), representative of SVOCs found in biogenic (four α-pinene oxidation products) and biomass burning (four polyaromatic hydrocarbons and biomass burning primary organic aerosol compounds) air mass types. The species in both SVOC subsets cover a range of pure species liquid saturation vapor pressures ($p^{o,L}$; estimated using the Estimation of Vapour Pressure of Organics, Accounting for Temperature, Intramolecular, and Nonadditivity effects model by *Compernolle et al.* [2011]); at 298.15 K the SVOC $p^{o,L}$ values range from 10^{-11} to 10^{-2} Pa. Two organic compounds, docosanoic acid

Table 1. Initialization Data Used for the Thermo-Kinetic Model Simulations

Parameter	Value
Ambient Conditions	
Temperature[a]	250, 295, 310 K
Relative humidity	60%
Aerosol Particles	
Initial Composition (by mass)	
$\quad$NH$_4$NO$_3$	30%
$\quad$(NH$_4$)$_2$SO$_4$	20%
$\quad$Mixed SVOCs	50%
Aerosol concentration	5 μg m^{-3}
Particle diameter	250 nm
Bulk Diffusivity (water)	
$\quad$Liquid	10^{-5} cm^2 s^{-1}
$\quad$Semi-solid	10^{-10} cm^2 s^{-1}
Bulk diffusivity (organic)	
$\quad$Liquid	10^{-7} cm^2 s^{-1}
$\quad$Semisolid	10^{-15} cm^2 s^{-1}
Instrument Conditions	
Drying RH	10%
Sampling RH[a]	75, 85, 93%
Internal temperature	300 K
Drying residence time	3 s
Wetting residence time	4 s

[a]Multiple values indicate all values used across separate modeling runs.

and "C15H18O7" (Table 2; a syringol derivative formed in aqueous secondary organic aerosol [*Yu et al.*, 2014]) comprised the low-volatility organic compound (LVOC) particle fraction. Ammonium sulfate was used as a representative particle-phase inorganic species (considered nonvolatile).

Initial equilibrium concentrations were calculated at a reference temperature of 250 K and 60% RH, by assuming 5 μg m^{-3} of particulate matter with monodisperse spherical diameters of 250 nm, with an initially fixed composition (mass-%) of 5% ammonium nitrate, 25% ammonium sulfate, 50% low-volatility organic compounds (4:1 mixture of docosanoic acid and C15H18O7), and 20% semivolatile organic compounds (with the organic fraction composed of the subset species, evenly distributed by mass). For the semivolatile components, the corresponding gas-phase concentrations were then computed for the condition of gas-particle equilibrium. The goal of this initial procedure is to determine the total (gas + particle) molar amounts of all the organic and inorganic system components per unit volume of air. All calculations at different temperatures and various RH levels were then performed using the same total molar concentrations (per cubic meter of air) after equilibration at the varied modeling conditions (i.e., particle phase organic composition was not held fixed at original reference conditions). It is recognized that the initial species composition chosen for the model is not specifically representative of the composition of all air masses measured during the SEAC[4]RS campaign and that the simulation results should represent an upper limit of potential semivolatile losses within the DASH-SP instrument.

Table 2. Selected SVOC, LVOC, and Inorganic Compound Properties Used for the Thermo-Kinetic Model Simulations

Name	MW(g mol^{-1})	p^{o,L} (298.15 K)(Pa)	Composition
Inorganic			
Ammonium sulfate	132.14		(NH$_4$)$_2$SO$_4$
Ammonium nitrate	80.04		NH$_4$NO$_3$
Semivolatile (Biogenic)			
C8H14O6	206.19	3.2262E-07	C$_8$H$_{14}$O$_6$
Pinonic acid	184.23	1.5341E-02	C$_{10}$H$_{16}$O$_3$
Pinic acid	186.21	4.7359E-05	C$_9$H$_{14}$O$_4$
Ester dimer[a]	368.42	2.6253E-11	C$_{19}$H$_{28}$O$_7$
Semivolatile (Biomass Burning)			
C8H12O6	204.18	6.2457E-06	C$_8$H$_{12}$O$_6$
Chrysene	228.29	5.2142E-03	C$_{18}$H$_{12}$
C22H12	276.33	2.3903E-05	C$_{22}$H$_{12}$
Abietic acid	302.45	5.3520E-06	C$_{20}$H$_{30}$O$_2$
Low-Volatility Organic Compounds			
Docosanoic acid	340.58	9.1507E-08	C$_{22}$H$_{44}$O$_2$
C15H18O7	310.30	1.2362E-10	C$_{15}$H$_{18}$O$_7$

[a]Ester dimer formation from hydroxypinonic acid and pinic acid.

Particle mass losses are reported as normalized species mass (i.e., percentage of initial species mass remaining) in Figure 3. Evaporation behavior was investigated as a function of ambient temperature (250 K, 295 K, and 310 K; representative of a range of tropospheric altitudes), sampling RH (75%, 85%, and 93%), and physical state of aerosol particle phase (liquid and semisolid). The volatility of SVOCs is more sensitive to a change in temperature difference (i.e., instrument-ambient) than a change in sampling RH. For instance, ammonium nitrate is shown to lose 65.7%, 61.2%, and 56.5% of its original mass due to volatilization at sampling RH values of 75%, 85%, and 93%, respectively, at a fixed ambient
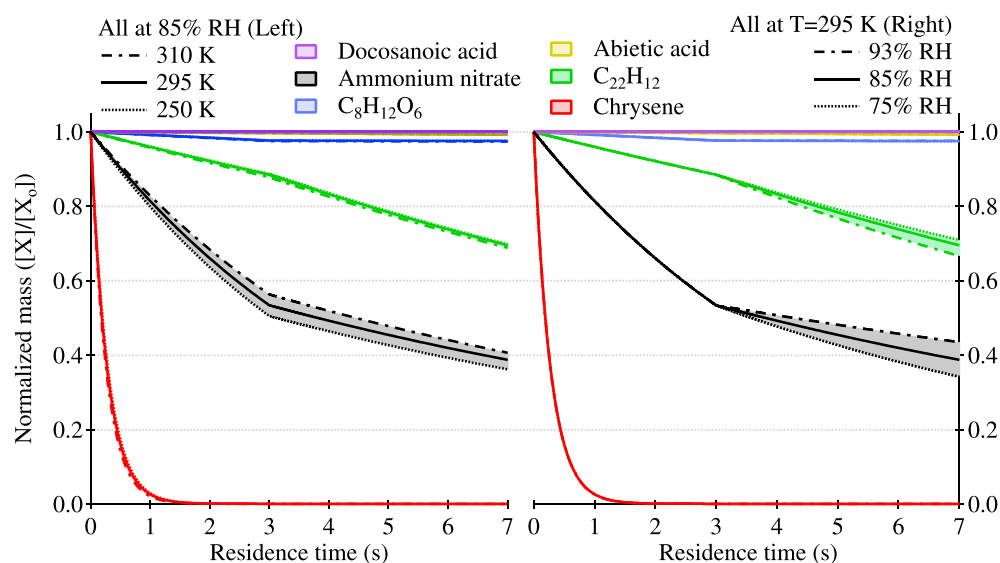
Figure 3. Thermo-kinetic modeling results of selected semivolatile species losses in the range of sampling conditions encountered during SEAC4RS. (a) Simulation results for ambient temperatures of 250, 295, and 310 K, all at a constant instrument temperature of 300 K and RH of 85%. (b) Simulation results at a fixed ambient temperature of 295 K, and with instrument RH values of 75, 85, and 93% that were commonly used during SEAC4RS. Data shown are modeled assuming liquid particle phase properties as described in section 3.

sampling temperature of 295 K. When constraining the sampling RH value to 85%, and running the model at ambient temperatures of 250 K, 295 K, and 310 K, evaporative losses of ammonium nitrate were 63.8%, 61.2%, and 59.3%, respectively. The percentage of original mass lost for organics ranged between ~0 (e.g., docosanoic acid) and ~100% (e.g., chrysene) depending mainly on the species pure component volatility at the experimental conditions.

For 250 nm diameter particles with a liquid (low-viscosity) particle phase, mass transport within the condensed phase is very rapid. When the particle phase is semisolid, the bulk diffusivity of water and organics [*Shiraiwa et al.*, 2011, 2013] is reduced by 2 to 5 orders of magnitude. This increases the time scales of the transient evaporation and condensation processes of both water and organics required to reach a new equilibrium state. Based on the modeling parameters chosen to best represent liquid and semisolid phase conditions, the water evaporation and condensation processes reach equilibrium during the residence time for each stage and both phase conditions. However, when aerosol particles take on a semisolid particle phase, losses of SVOCs and ammonium nitrate are reduced in both stages of the DASH-SP by a factor of 5 or more. For example, at 295 K and a sampling RH of 85%, the loss of ammonium nitrate is reduced from 61.2% (liquid particle phase) to 0.1% (semisolid particle phase).

The impact to the overall GF is determined by the change in particle diameter due to both volatility losses and condensation of water and SVOCs. For the composition used in this simulation, the GF at 85% RH is reduced from 1.15 (no SVOC losses) to 1.11 (with SVOC losses) at 250 K and from 1.17 to 1.15 at both 295 K and 310 K. These values provide a sense of the upper limits of how much the GFs reported here could be underestimated relative to a semivolatile ambient aerosol.

4. Results and Discussion

4.1. Statistical Summary of Results

To place the upcoming hygroscopicity results in perspective, Figure 4 shows both the average LAS number size distributions for each air mass and the normalized Mie scattering intensity for a representative category (BB-Wildfires). The latter is to show that the DASH-SP size range effectively captures the diameter range where scattering is most intense for the BB-Wildfires category (also applies to other categories, although not shown in Figure 4) with the modal diameter of most efficient scattering ranging from 275 to 375 nm. The strongest plumes sampled, in terms of number concentration, were from the BB-Agricultural category, which exhibited the highest number concentration ($>$14,000 cm^{-3}) with a modal diameter of ~130 nm.
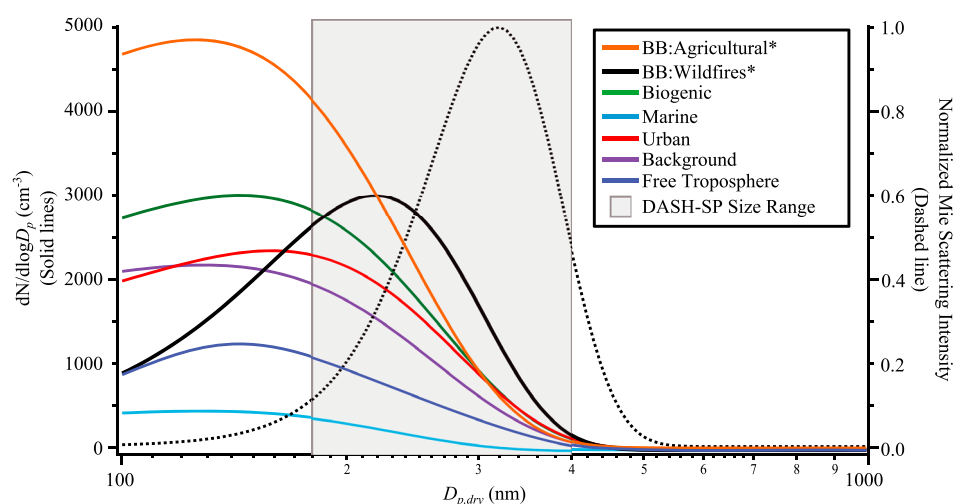
Figure 4. Average LAS size distributions for individual air mass types (* = trace scaled by one third for clarity). The dashed line represents the normalized Mie scattering (for $RI_{dry} = 1.54$) intensity associated with a dry particle size distribution equivalent to the average BB-Wildfire distribution (solid black line). The SEAC[4]RS dry size sampling range of the DASH-SP instrument is indicated in the gray rectangle.

The category with the next highest number concentration was BB-Wildfires, which also exhibited the largest modal diameter in its number size distribution among all air types studied (~225 nm). The other air types exhibited modal diameters between 100 and 200 nm and with lower particle number concentrations.

Overall statistics for hygroscopicity and RI_{dry} parameters are reported in Figure 5 as a function of air mass type. GF values are averaged at sampling RH values of 75, 80, 85, 90, and 95% (all ±2.5%), while κ_{GF} values (derived from DASH-SP GF measurements using equation (1)) incorporate data from all sampling RH values. DASH-SP data in Figure 5 are for measurements with $D_{p,dry}$ between 188 and 312 nm. To facilitate a hygroscopicity comparison between the DASH-SP and the f(RH) measurement, results displayed in this section are limited to concurrent sampling times between both instruments. Detailed numerical statistics for Figure 5 data (average, standard deviation, minimum, and maximum) can be found in Table S1 in the supporting information.

κ_{GF} is highest for marine aerosol (0.38 ± 0.13) as compared to the other continentally derived air masses including urban (0.28 ± 0.12), BB-Wildfires (0.11 ± 0.05), BB-Agricultural (0.12 ± 0.05), biogenic (0.21 ± 0.08), background (0.24 ± 0.11), and FT (0.23 ± 0.11). Other work has also shown that hygroscopicity of marine aerosol is enhanced relative to urban and continental air masses, the latter including mineral dust and biomass burning [e.g., *Carrico et al.*, 1998, 2000, 2003; *Kotchenruther and Hobbs*, 1998; *McInnes et al.*, 1998; *Gasso et al.*, 2000; *Sheridan et al.*, 2001; *Kim et al.*, 2006; *Zieger et al.*, 2011, 2012]. The lowest κ_{GF} standard deviation values were for the biomass burning categories (±0.05) due presumably to the short-lived nature of the plumes sampled near their source, which prevented additional aging and changes in physicochemical properties. Negative values of κ_{GF} are associated with observed sub-1.0 GFs that are outside the uncertainty of the measurement and may potentially be explained by particle collapse upon hydration resulting in shrinkage of the apparent optical diameter [*Weingartner et al.*, 1997; *Jimenez et al.*, 2003]. These low GF values are primarily observed during sampling of biomass burning smoke, thus potentially contributing to the lowest κ_{GF} observations. A future study focused on sub-1.0 GF observations, including data from this study and other field sampling, is forthcoming.

To further address the issue previously noted about absorption affecting the DASH-SP OPC response, single scattering albedo (SSA), as derived from the LARGE package, of biomass burning plumes from wildfires was quantified and compared to values in the literature. The average SSA was 0.96 ± 0.01, which exceeds that of other studies of wildfire plumes and is consistent with values in the range of 0.91–0.99 that coincide with more aged particles [*Corr et al.*, 2012, and references therein]. Therefore, we interpret the SSA values as being supportive of absorption not having significantly impacted OPC behavior.

The lowest variability in average GF values was noted for BB-Wildfires, with a range of standard deviations between ±0.05 and ±0.06 across all sampled RH settings, while the greatest variability was observed for the background (±0.10 to ±0.12) and FT (±0.09 to ±0.14) categories. GF values increase monotonically as a
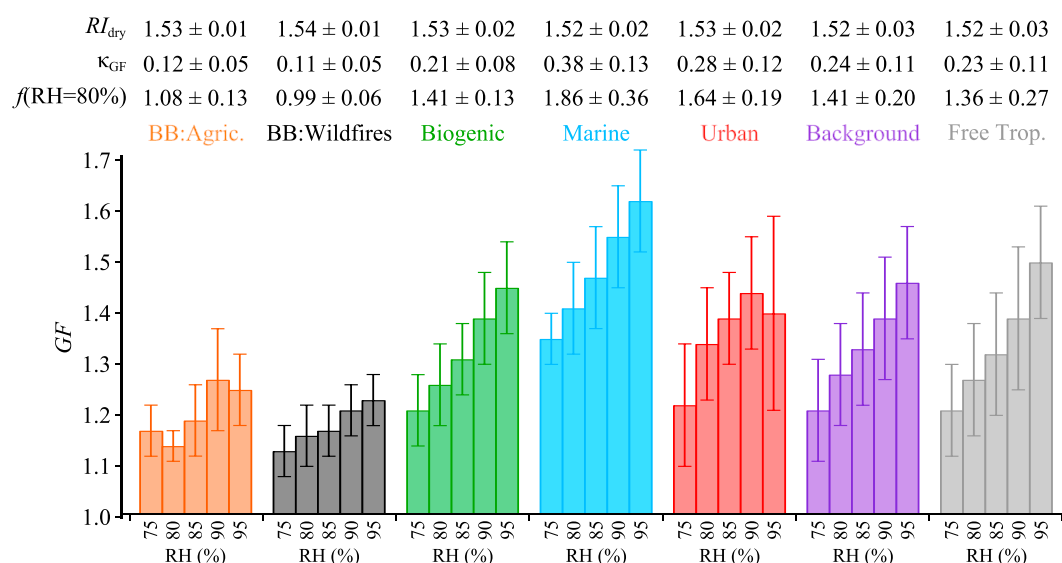
Figure 5. Summary of DASH-SP GF, RI_{dry} (at 532 nm), and κ_{GF} values as a function of air mass type and sampling RH for $D_{p,dry}$ values between 188 and 312 nm. Bulk aerosol f(RH = 80%) results for the same air mass classifications are also shown. GF error bars and plus-minus sign values in the three rows of data represent 1 standard deviation. Data are limited to concurrent, valid sampling periods between both the DASH-SP and LARGE f(RH) measurements.

function of sampling RH between 75 and 95% for all air mass classifications except BB-Agricultural ($GF_{80\%} < GF_{75\%}$) and urban ($GF_{95\%} < GF_{90\%}$). The explanation for these two situations is most likely due to the limited opportunities to sample in these categories, and thus, specific agricultural fires or urban areas could have been sampled more or less at a certain sampling RH condition. A case study for the urban category is presented later (section 4.5) for a flight probing Los Angeles aerosol on 23 September 2013.

Bulk aerosol f(RH = 80%) values are in agreement with κ_{GF} values in terms of relative differences between various air mass classifications (e.g., higher for marine and lowest for BB categories). The BB categories exhibited the narrowest range and variability in f(RH), while marine exhibits the highest variability (±0.36), similar to κ_{GF}. It is possible that this variability was introduced by potentially misclassified measurements above the marine boundary layer.

Chemical composition data are consistent with the hygroscopicity trends in Figure 5. Submicron aerosol species mass fractions (MFs) and mass concentrations were averaged across the different air mass types and are shown in Figure 1. Both BB air types were dominated by organics (OA) with low sulfate and high BC ($MF_{OA} = 89\%$, $MF_{sulf} = 2\%$, and $MF_{BC} = 2\%$), which is consistent with reduced hygroscopicity as compared to other air mass types. Compared to other air mass types, the much higher mass concentrations for BB-Agricultural are consistent with Figure 4 that showed these plumes were very fresh with high particle number concentrations in the DASH-SP sampling range. Marine air masses exhibited the highest inorganic (IOA) mass fractions, dominated mainly by sulfate with lower organic and BC content ($MF_{OA} = 21\%$, $MF_{sulf} = 65\%$, and $MF_{BC} = 1\%$), which can explain the enhanced hygroscopicity for this category. The urban, biogenic, background, and free troposphere air mass categories exhibited chemical signatures similar to each other with intermediate organic mass fractions and low BC fractions ($MF_{OA} = 56$–64%, $MF_{sulf} = 25$–34%, and $MF_{BC} \leq 1\%$), coinciding with intermediate hygroscopic properties relative to BB and marine air types.

An interesting finding from SEAC[4]RS was that average RI_{dry} values for all air mass classifications were quite similar with a narrow range of 1.52–1.54, similar to pure inorganic species RI values of ammonium sulfate (1.521 [*Weast*, 1987]) and sodium chloride (1.544 [*Li*, 1976]), as well as in line with values currently used in many models [*Koepke et al.*, 1997]. Work by *Rickards et al.* [2013] has also shown similar RI values for a variety of pure organic species; including galactose (1.55), sorbitol (1.53), and xylose (1.52). The greatest standard deviations in RI_{dry} values were observed for the background and FT classifications (±0.03), while the BB categories exhibited the lowest standard deviations (±0.01). Minimum and maximum RI_{dry} values for all measurements were 1.42 and 1.60.
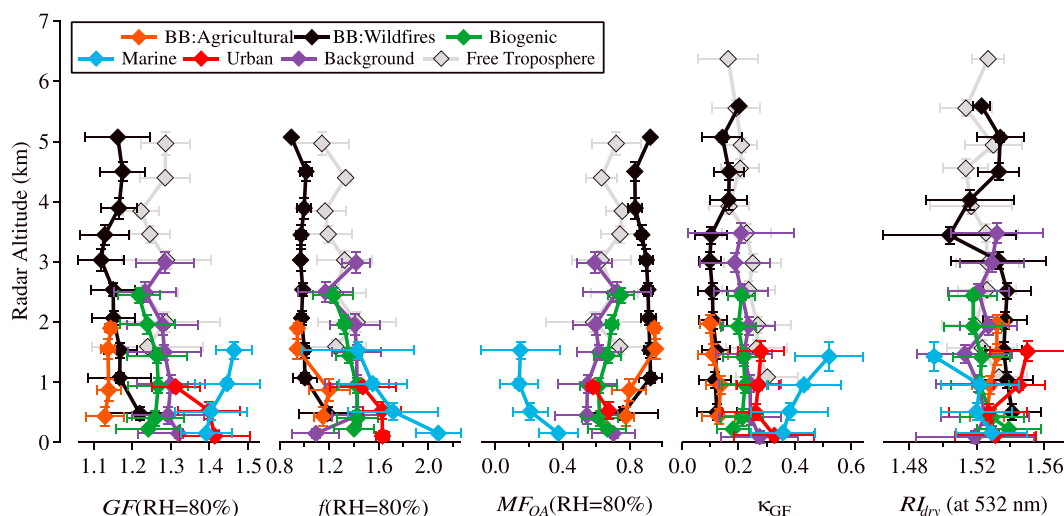
Figure 6. Vertical profiles of aerosol particle properties for individual air mass categories. GF(RH = 80%) from DASH-SP, f(RH = 80%) from LARGE, and MF$_{OA}$ from HR-AMS are all limited to only concurrent measurements. κ_{GF} and RI$_{dry}$ (at 532 nm) are shown for all DASH-SP sampling RH values. Error bars indicate 1 standard deviation.

4.2. Vertical Profiles of Hygroscopicity and Refractive Index

To analyze vertical profiles of aerosol hygroscopicity, data points were separated by air mass type and binned in 500 m altitude increments. The vertical profiles were constructed from average values using cumulative SEAC^{4}RS data during ascents, descents, and level legs. Coincident measurements (~20% of total valid DASH-SP scans) of GF (only at RH = 80%), f(RH = 80%), and MF$_{OA}$ were compared to one another, while κ_{GF} and RI$_{dry}$ (at 532 nm) were analyzed for all RHs examined by the DASH-SP (Figure 6). Valid DASH-SP scans were reported as high as 6.5 km above surface level, and the primary limiting factor above this height was insufficient particle concentrations to pass the quality control threshold.

Relative differences in hygroscopicity between air types in individual altitude bins follow trends from Figure 5 (i.e., highest for marine and lowest for BB). Except for the marine and FT categories, relatively minor variations in bin-mean hygroscopicity parameters were observed as a function of altitude. For example, bin-mean values of κ_{GF} are between 0.04 and 0.10 from near the surface to their highest-altitude bin points for all air mass categories. For the marine category, κ_{GF} increased by 0.16 (from 0.36 to 0.52) between 0.2 and 1.5 km, which is consistent with the reduction of MF$_{OA}$ with altitude by approximately a factor of 2. This result supports those of *Hegg et al.* [2006], who also showed that hygroscopicity increased with altitude in marine air, with the caveat that the SEAC^{4}RS data reach higher altitudes than their study. FT κ_{GF} values decreased from 0.30 to 0.16 from 1.1 km to 6.4 km, which coincides with an increase in MF$_{OA}$ from 0.36 to 0.83 (not shown). Other than the FT category, only the BB-Wildfires category exhibited data above 5 km owing to high-altitude transport of such plumes. κ_{GF} for this category was highest above 4 km, which could be explained due to aging effects where hygroscopic secondary species can form in aging smoke plumes [e.g., *Reid et al.*, 2005; *Maudlin et al.*, 2015]. Although not shown in the figure, this is supported by an increase in the average ratio of atomic oxygen to carbon (O:C) from 0.61 ± 0.09 (below 4 km) to 0.76 ± 0.09 (from 4 to 6.5 km).

While the bin-mean values of hygroscopicity do not vary significantly with altitude, the standard deviation in each altitude bin is considerable. The maximum κ_{GF} standard deviation among altitude bins for each air mass type ranges from as low as 0.06 (BB-Agricultural) to as high as urban (0.20).

With the exception of the marine category, altitude-dependent hygroscopicity trends largely are consistent between DASH-SP GF(RH = 80%) and f(RH = 80%). Between 0.2 and 1.5 km for the marine category, the average f(RH = 80%) value decreases from 2.08 ± 0.18 to 1.43 ± 0.45, while GF(RH = 80%) increases from 1.39 ± 0.07 to 1.46 ± 0.05. Although f(RH) data with substantial supermicron aerosol have been removed to allow for a fair comparison with AMS and DASH-SP data, the difference in the trends between GF and f(RH) may still be related to the bulk nature of the f(RH) measurement. The reduction in MF$_{OA}$ from 0.38 to 0.15 between 0.15 and 1.5 km, respectively, supports the GF(RH = 80%) trend with altitude since an inverse relationship is expected between
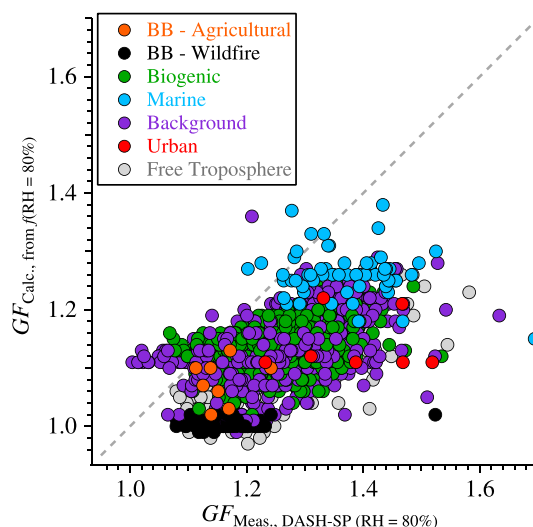
Figure 7. Comparison of GF$_{calc}$ versus GF$_{meas}$ as a function of air mass classification (represented by color-coding). Data shown are limited to concurrent sampling between the DASH-SP (only measurements at RH = 80%) and f (RH = 80%). To reduce the bias of supermicron particles on total scattering, only data are used where no counts above 1 μm diameter were detected by the LAS instrument.

organic fraction and GF. Previous airborne measurements in marine air have shown that GF is highest at an intermediate diameter between 300 and 700 nm with reductions outside both ends of this range owing to effects such as organic-rich aerosol and oxidation of organic films [*Hegg et al.*, 2006; *Hersey et al.*, 2011; *Coggon et al.*, 2014]. Thus, it is possible that f(RH) may have been influenced by aerosol with reduced hygroscopicity outside the size range of the DASH-SP.

RI$_{dry}$ values also exhibited minor variations with altitude for most air categories with the greatest ranges being for the biogenic (1.50–1.54) and marine categories (1.50–1.53), supporting the model values from the GADS look-up tables [*Koepke et al.*, 1997], with decreases as a function of altitude for both. The urban and background air categories were the only two to exhibit increases in RI$_{dry}$ with altitude, with the former exhibiting the highest overall value (1.55) in Figure 6 at its peak altitude of 2.4 km. The standard deviation maximum ranges from a minimum of 0.01 (BB-Agricultural) to a maximum of 0.04 (BB-Wildfire and background).

4.3. GF and f(RH) Intercomparison

As noted above, the simultaneous f(RH) and GF airborne data allow for an evaluation of whether a relationship can be developed between the two data sets to help link f(RH) more directly to model parameterizations of hygroscopic growth (e.g., κ). A comparison was performed using data when both instruments were simultaneously operating at 80% RH. Figure 4 has already emphasized that the f(RH) measurement is weighted toward sizes larger than the mode of the number size distribution. For this analysis, data were limited only to those with negligible contribution from coarse particle sizes (i.e., particle concentrations were zero above 1 μm). The GF-f(RH) comparison was performed by determining a calculated f(RH) value (f(RH)$_{calc}$) from the measured dry aerosol size distribution, Mie scattering theory, and an assumed (size-independent) GF value (GF$_{calc}$) [*Cappa et al.*, 2011; *Zhang et al.*, 2014]. The GF$_{calc}$ value was iterated until the f(RH)$_{calc}$ value was equivalent to the measured f(RH = 80%) measurement (± < 1%). This approach allowed for the determined GF$_{calc}$ value to be compared directly to the GF value measured by the DASH-SP instrument (GF$_{meas}$).

Comparison of GF$_{calc}$ and GF$_{meas}$ indicates that the growth of particles measured by the DASH-SP is underestimated by the predicted value derived from the bulk f(RH) measurement for all air mass types (Figure 7). Deriving a κ value from f(RH), via a fixed GF$_{calc}$, is a convenient way to relate the growth of a dry aerosol size distribution to bulk aerosol light scattering; however, if hygroscopicity is not homogeneous across the size distribution, it may not accurately represent the physical growth characteristics of particles at discrete sizes.

One explanation for the discrepancy between the two measurements is that particles outside the DASH-SP size range were less hygroscopic, as has already been suggested in section 4.2. To form an agreement between the two measurements, the κ values of larger sized particles would need to range in value from approximately the value determined by the DASH-SP to as low as zero (or lower if particle shrinkage is detected by the f(RH) measurement). This would apply to particles with $D_{p,dry} > 250$ nm as most (94.4%) of the DASH-SP scans were for $D_{p,dry} \leq 250$ nm. To investigate the dependence of hygroscopicity on size, coincident measurements between the DASH-SP, LARGE, and HR-AMS were compared to the modal D_p of the LAS number size distribution (Figure 8). GF(RH = 80%) and f(RH = 80%) decrease (1.31–1.16 and 1.33–1.02, respectively) with increasing modal D_p (from 100 to 251 nm). While the modal D_p values do not extend beyond the
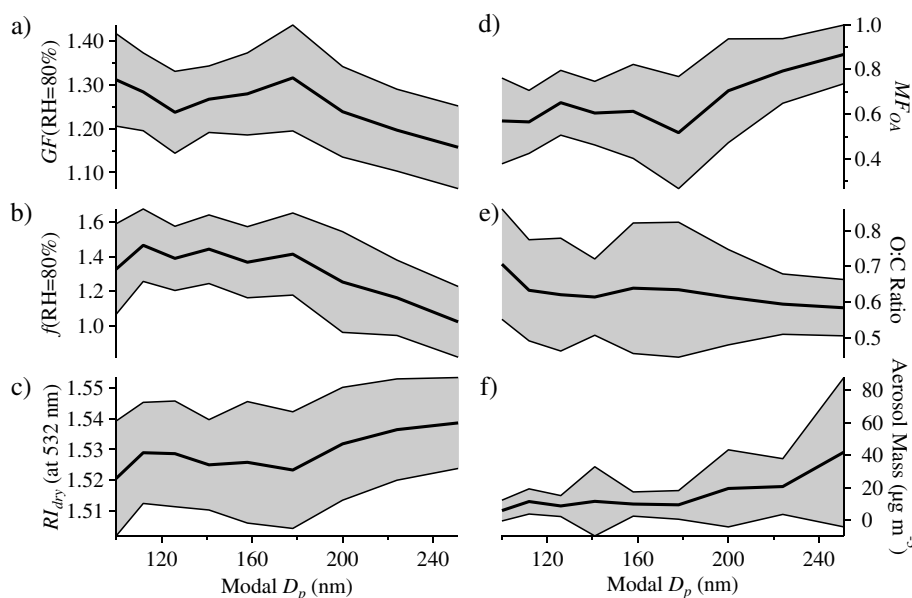
Figure 8. Size-dependent average values (shaded areas signify 1 standard deviation) of (a) DASH-SP GF, (b) LARGE f(RH), (c) DASH-SP RI_{dry} (532 nm), (d) HR-AMS MF_{OA}, (e) HR-AMS O:C ratio, and (f) HR-AMS total submicron non-refractory mass concentration. Modal D_p values were obtained from the LAS instrument. Although not shown, the trends as a function of LAS modal D_p match those with the ratio of the number concentration above 200 nm relative to total number concentration. Data are limited to concurrent, valid sampling periods between both the DASH-SP and LARGE f(RH) measurements at 80% RH.

size range of the DASH-SP, the decreasing trend in hygroscopicity with modal D_p in Figure 8 suggests that the proposed explanation above is at least plausible. It is noted that by using modal D_p, the analysis in Figure 8 disregards variability in a given size distribution, but the trend of hygroscopicity with modal D_p is consistent with an independent analysis discussed next in Figure 9.

A case flight on 19 August 2013 further examines the dependence of hygroscopic growth on particle size as it included a wide range of $D_{p,dry}$ values (180–305 nm) sampled across the entire flight (Figure 9). A clear result emerges that larger particles (in the range of the DASH-SP) exhibit decreased hygroscopicity, including within specific air mass categories. Thus, the heterogeneity of hygroscopic properties over an aerosol size distribution should be taken into account when converting total scattering measurements to hygroscopicity parameters such as κ.
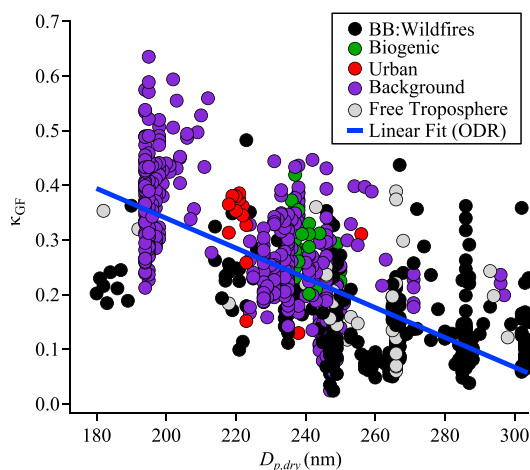
Figure 9. κ_{GF} as a function of $D_{p,dry}$ based on all DASH-SP data on 19 August 2013. Markers are colored with air mass classification. A linear orthogonal distance regression (ODR) fit is shown in blue.

4.4. Relationship Between Composition and Hygroscopicity

Particle water-uptake properties are highly sensitive to the amount of organic material present in the aerosol phase. Higher OA mass fractions have been shown to lead to suppressed water uptake at RHs above the deliquescence RH (DRH) of salts, while simultaneously enhancing hygroscopic growth at RHs below the DRH [e.g., *Dick et al.*, 2000; *Hersey et al.*, 2009; *Meyer et al.*, 2009]. Furthermore, aging of organic aerosol to convert organic compounds from less to more oxidized forms can enhance GFs [e.g., *Jimenez et al.*, 2009; *Massoli et al.*,
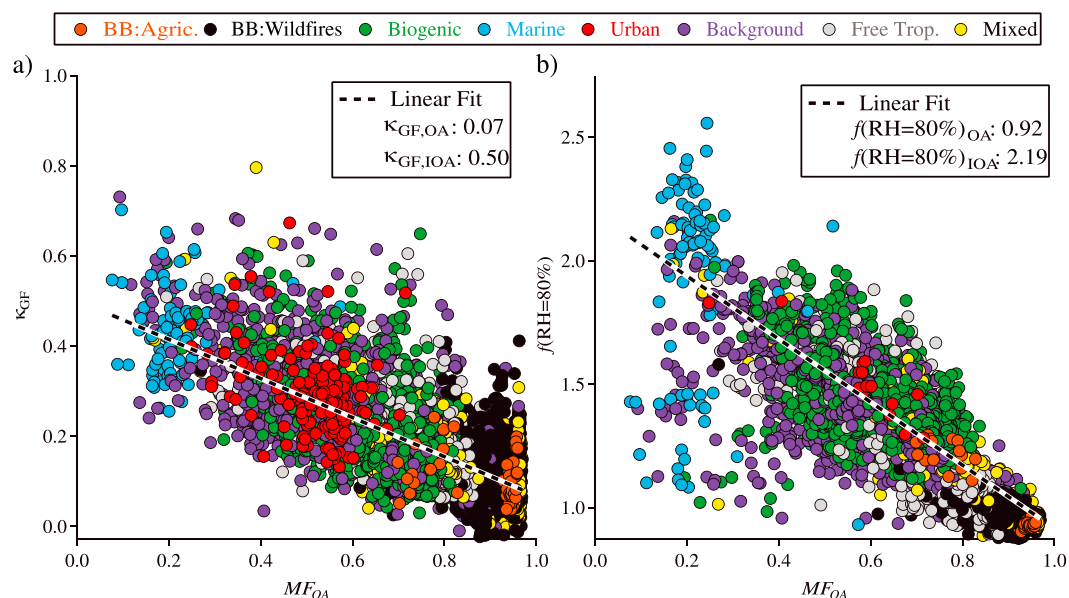
Figure 10. (a) DASH-SP κ_{GF} and (b) LARGE $f(RH = 80\%)$ plotted against MF_{OA} measured by the HR-AMS. Linear fits in each panel show how $\kappa_{GF,OA}$ and $f(RH = 80\%)_{OA}$ values were derived, which are used as proxies for hygroscopicity at the limit of total organic composition (i.e., $MF_{OA} = 1$). Conversely, values for the inorganic counterparts are determined at the limit of total inorganic composition (i.e., $MF_{OA} = 0$).

2010; *Duplissy et al.*, 2011; *Wonaschütz et al.*, 2013], where the level of organic oxidation is typically represented by the O:C ratio. Measurements have indicated that more hygroscopic aerosols (at fixed RH and $D_{p,dry}$) enhance aqueous-phase chemistry to generate secondary aerosol mass [*Sorooshian et al.*, 2010; *Youn et al.*, 2013], and thus, a two-way relationship exists between hygroscopicity and chemistry.

Figure 10 confirms that both κ_{GF} and $f(RH = 80\%)$ are inversely related to MF_{OA}. Fitting a linear function to κ_{GF} and taking the value at $MF_{OA} = 1$ results in a $\kappa_{GF,org}$ value, which is an indication of the hygroscopic nature of the organic aerosol fraction. The κ_{OA} value is frequently used in models like the Zdanovskii-Stokes-Robinson (ZSR) [*Stokes and Robinson*, 1966] model to predict hygroscopicity based on chemical composition data [e.g., *Wu et al.*, 2013]. Previously derived κ_{OA} values range between 0.0 and 0.4 [*Petters and Kreidenweis*, 2007; *Suda et al.*, 2012; *Rickards et al.*, 2013; *Brock et al.*, 2015] and have been shown to be positively correlated to the O:C ratio [*Jimenez et al.*, 2009]. An overall $\kappa_{GF,OA}$ value for the SEAC[4]RS campaign was found to be 0.07 and very similar to $\kappa_{ext,OA}$ values determined for the southeastern United States by *Brock et al.* [2015], using a separate
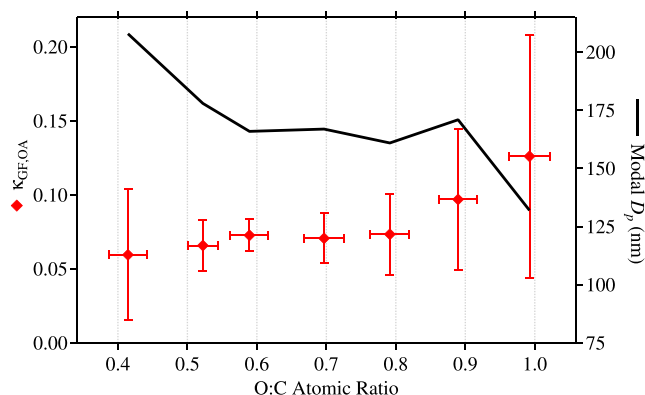
Figure 11. Dependence of $\kappa_{GF,OA}$ and LAS modal D_p values on the HR-AMS O:C ratio. Data were binned by O:C ratio using 0.1 bin widths. Average O:C values within the bins are plotted with 1 standard deviation represented by horizontal error bars.
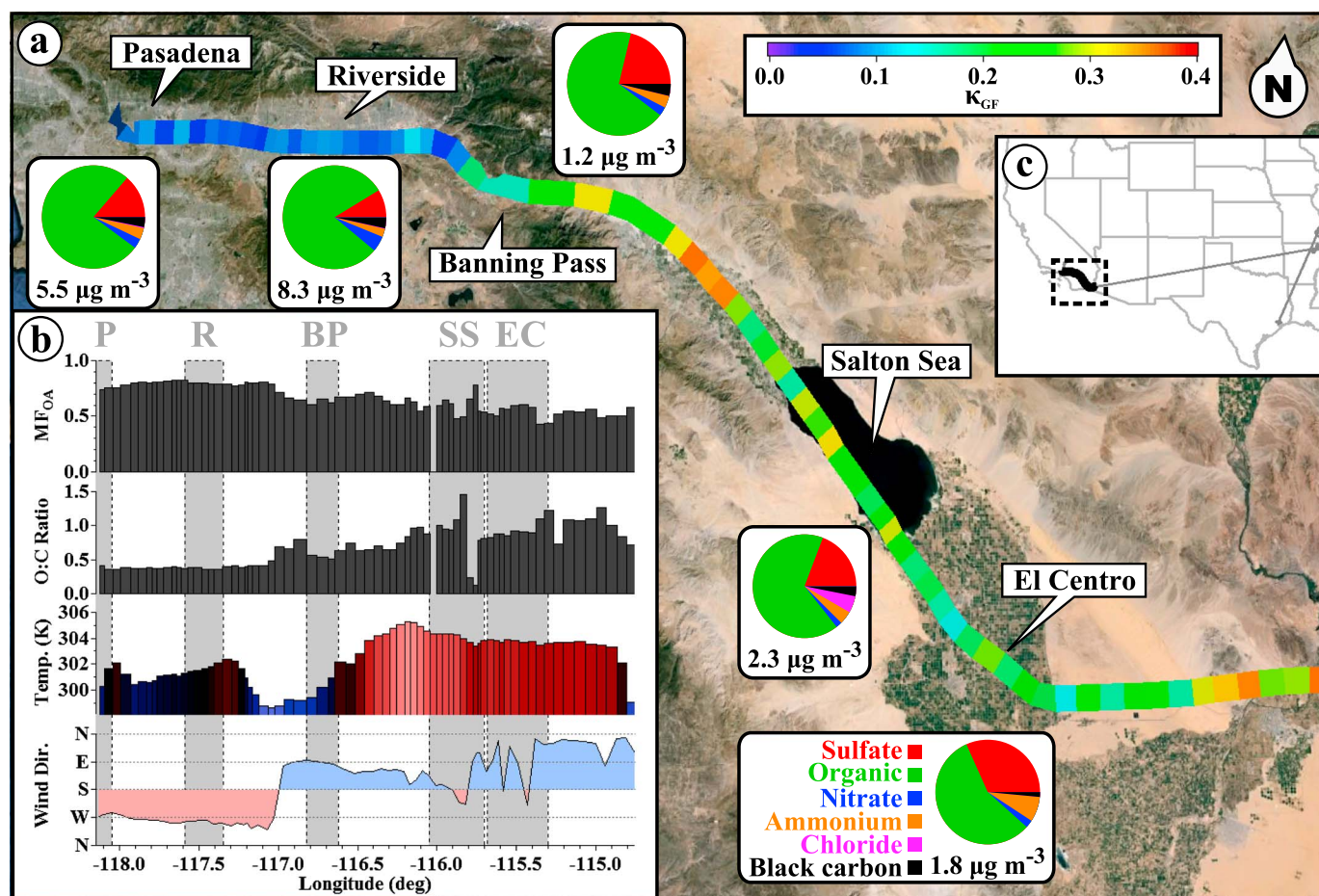
Figure 12. (a) Flight track from El Centro to Los Angeles, California, on 23 September 2013 between approximately 15:55 and 16:40 local time. The flight track is color-coded with κ_{GF} at a fixed $D_{p,dry}$ of 195 ± 2 nm, with the DASH-SP instrument RH cycling between 77 and 95%. Key landmarks along the flight path are indicated on the map and represented in the inset plots as gray boxes (e.g., El Centro = "EC" and Riverside = "R"). Aerosol species mass fractions are shown in pie charts along with total mass concentration (below pies) corresponding to data averaged over periods shown in the gray boxes. Inset (b) contains MF_{OA} and O:C ratio from the HR-AMS instrument, ambient temperature (color is only a function of the y-axis value for emphasis), and wind direction (blue is from the east, red is from the west). A small map with wider field of view (c) is shown to provide a sense of where the flight track was relative to neighboring areas.

approach. (Note, that their $\kappa_{ext,OA}$ parameter is derived from considerations of κ-Köhler theory and f(RH) measurements.) The $\kappa_{GF,IOA}$ value (i.e., when $MF_{OA} = 0$) was found to be 0.50. It is cautioned that although the overall nitrate signal from the HR-AMS is generally a small fraction of the total aerosol, a portion of the nitrate signal is from organic nitrate. Values for f(RH = 80%)$_{OA}$ and f(RH = 80%)$_{IOA}$ were 0.92 and 2.19, respectively. Note that an f(RH) value of 0.92 suggests that wetted particles scatter less light than dried particles as seen in the highly organic biomass burning classification. While restructuring of soot spherules may physically account for this phenomenon, further work is needed to elucidate both measurements uncertainties as well as chemical mechanisms that would result in f(RH) < 1.

At a specific MF_{OA} value in Figure 10, it is evident that there is a range of hygroscopicity for a given air mass, which may be related to the nature of the organic fraction. To probe deeper, Figure 11 shows how $\kappa_{GF,OA}$ is related to the O:C ratio, using bin widths of 0.1 for the latter. There is an increase in $\kappa_{GF,OA}$ (from 0.06 ± 0.04 to 0.13 ± 0.08) as a function of the O:C ratio between 0.4 and 1.0, coincident with a decrease in the modal D_p of the LAS number size distribution. This indicates that aerosol with smaller modal D_p values exhibited a more oxidized and hygroscopic organic fraction based on DASH-SP measurements. The air mass types with the highest O:C ratios were marine (0.93 ± 0.30) and FT (0.90 ± 0.30) with the others being 0.65 ± 0.22 (urban), 0.65 ± 0.16 (background), 0.63 ± 0.10 (BB-Wildfires), 0.57 ± 0.06 (biogenic), and 0.48 ± 0.10 (BB-Agricultural).
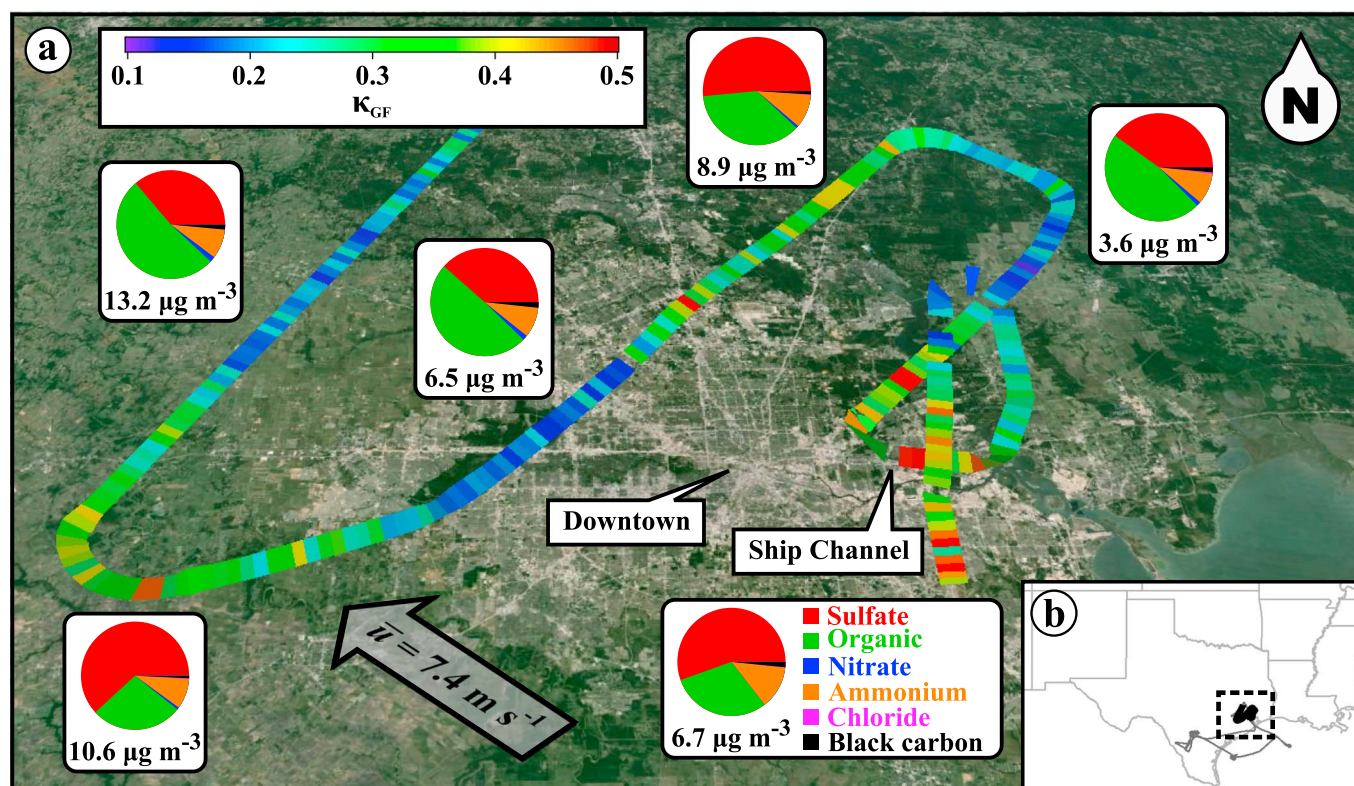
Figure 13. (a) Flight track over Houston, Texas, on 18 September 2013 between approximately 16:00 and 16:45 local time, color-coded with DASH-SP κ_{GF}. Aerosol species mass fractions and average total mass concentrations are shown in pie charts. Average wind speed ($\bar{u}$) and direction are indicated with the gray arrow. A small map with wider field of view (b) is shown to highlight where the flight track was relative to neighboring areas.

The results from Figures 9 and 10 can help explain trends in Figures 8c–8f, where MF_{OA} increases with modal D_p, coincident with enhancements in RI_{dry} and total submicron aerosol mass concentration, and reduced O:C ratios, as would be expected from the BB and biogenic categories.

4.5. Case Study: Urban Boundary Layer Comparison: Los Angeles, CA, and Houston, TX

Near the end of the flight on Monday, 23 September 2013, a low-level (<500 m) transect was performed between 15:55 and 16:40 local time from the city of El Centro, CA, over the Salton Sea, through Banning Pass, over Riverside, and ending near Pasadena (Figure 12). The DASH-SP sampled 195 nm diameter particles during this stretch at RH values cycling between 77 and 95%, with a resulting average RH of $90 \pm 5\%$. This bias toward sampling at a higher RH accounts for the dip in GF(RH = 95%) seen in Figure 5 for the urban air mass category (92% of data collected in the 95% RH bin were from the Los Angeles region).

East of the Los Angeles Basin, hygroscopicity was enhanced (κ_{GF} between 0.15 and 0.35) coincident with elevated MF_{sulf} (20 and 30%) and low total submicron mass concentration (1.2 and 2.3 $\mu g\,m^{-3}$), with a peak chloride concentration of 0.6 $\mu g\,m^{-3}$ over the Salton Sea. When flying into the Los Angeles Basin from the east, the wind direction changed from easterly to westerly and the total aerosol mass concentration ramped up to 8.3 $\mu g\,m^{-3}$. MF_{OA} increased to greater than 0.75 and κ_{GF} decreased to an average of 0.07 ± 0.02. The O:C ratio of the aerosol mass dropped from greater than 1.0 to approximately 0.6.

DASH-SP measurements were collected in nearly the same areas in 2010 during CalNex by *Hersey et al.* [2013]. They reported opposite trends in organic mass fractions and hygroscopic growth. In their flights, traveling west to east from the Los Angeles Basin, through Banning Pass, and out into the Imperial Valley, MF_{OA} increased (from approximately 0.42 to 0.65) and hygroscopicity dropped (κ_{GF} fell from 0.4 to 0.2). These changes were attributed to volatilization of ammonium nitrate to the east of Banning Pass in the desert areas [e.g., *Duong et al.*, 2011; *Metcalf et al.*, 2012]. During the SEAC⁴RS case study, the average temperature in the Los Angeles Basin (~301 K) and east of Banning Pass (~304 K) exceeded those experienced during CalNex (~289 K and
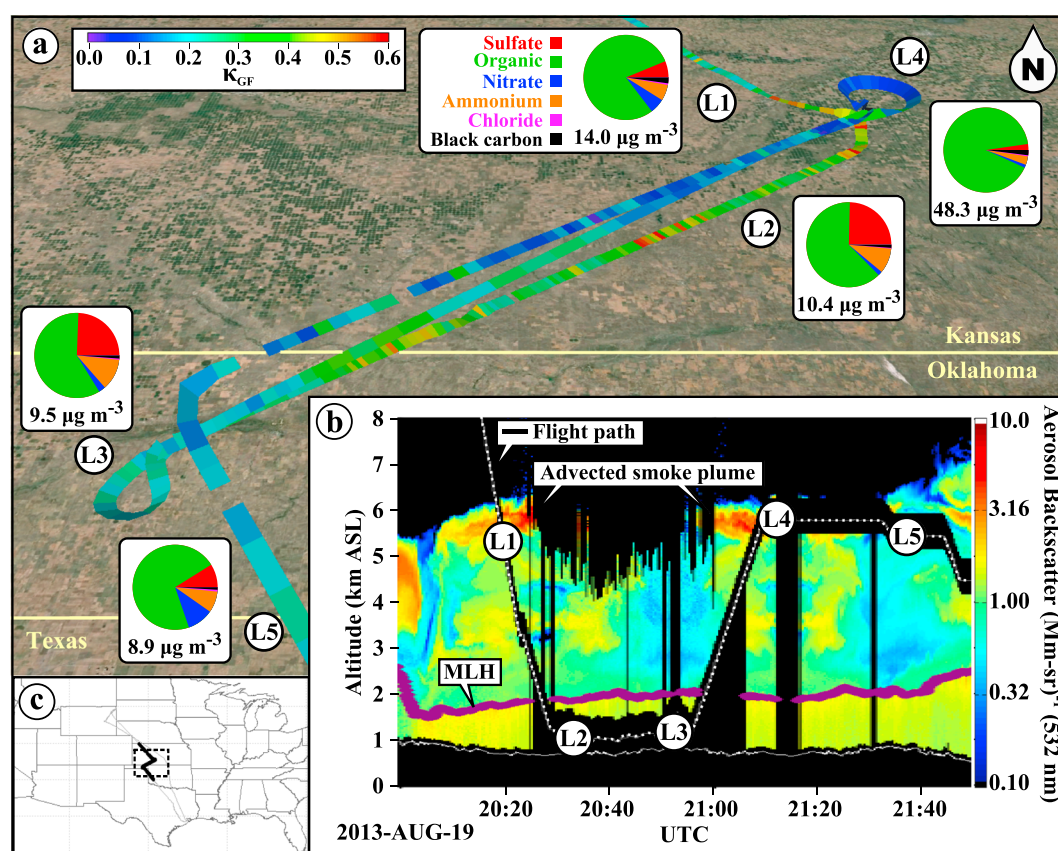
Figure 14. (a) Flight track over rural parts of southern Kansas and the Oklahoma panhandle on 19 August 2013 between approximately 15:10 and 16:45 local time, color-coded with DASH-SP κ_{GF}. Aerosol species mass fractions and average total mass shown in pie charts. Three in-line flight legs along a 50°/230° heading were used to create a wall pattern between approximately 1.1 km asl (in PBL) and 5.5 km asl (in transported smoke in FT). (b) Vertical curtain from the HSRL instrument showing aerosol backscatter at 532 nm. The transported smoke layer can be seen by the high scattering intensity at ~5.5 km asl. The height of the mixed layer, defined by the HSRL instrument, is indicated with the purple line in Figure 14b. Individual points along the flight path are denoted L1–L5 and correspond to the altitude profile in Figure 14b, inset. (c) A small map with wider field of view is shown to highlight where the flight track was relative to neighboring areas.

~297 K, respectively), and thus, volatilization still likely was at play. However, the CalNex flights were conducted earlier in the day (10:00–15:00 local time) when more ammonium nitrate would be expected in the Los Angeles Basin (i.e., sum of $MF_{nitrate}$ and $MF_{ammonium}$ was nearly 0.50); without the ammonium nitrate in the Basin aerosol during the SEAC[4]RS case study (i.e., the sum of $MF_{nitrate}$ and $MF_{ammonium}$ was only 0.07), there was no potential for it to volatilize and result in reduced hygroscopicity in the warmer outflow region to the east.

A similar style flight pattern was performed in the Houston, Texas, urban area on Wednesday, 18 September 2013 between 16:00 and 16:45 local time (Figure 13). The flight path included two passes perpendicular to the wind direction (127 ± 8° at 6.3 ± 1.9 m s^{-1}) downwind of the city, before passing over the Houston Ship Channel, and finally returning to the airfield. Two distinctly different regions were identified and denoted here as "Downtown" and "Ship Channel." Aerosol particles sampled downwind of the Downtown region exhibited higher MF_{OA} (50–55%) as compared to the Ship Channel (25–30%) and lower hygroscopic growth (κ_{GF} of 0.21 ± 0.05 versus 0.37 ± 0.11, respectively). Comparisons between the Los Angeles and Houston urban areas, at the same time of day (local time), indicate a more organic-rich PBL in the Los Angeles Basin resulting in lower absolute κ_{GF} values as compared to Houston.

4.6. Case Study: Characterization of Transported Smoke Aloft

The flight from Monday, 19 August 2013, already mentioned in Figure 9, is revisited here. Fresh wildfire emissions were sampled over northeastern Wyoming, as well as advected, aged, smoke in southern Kansas, originating
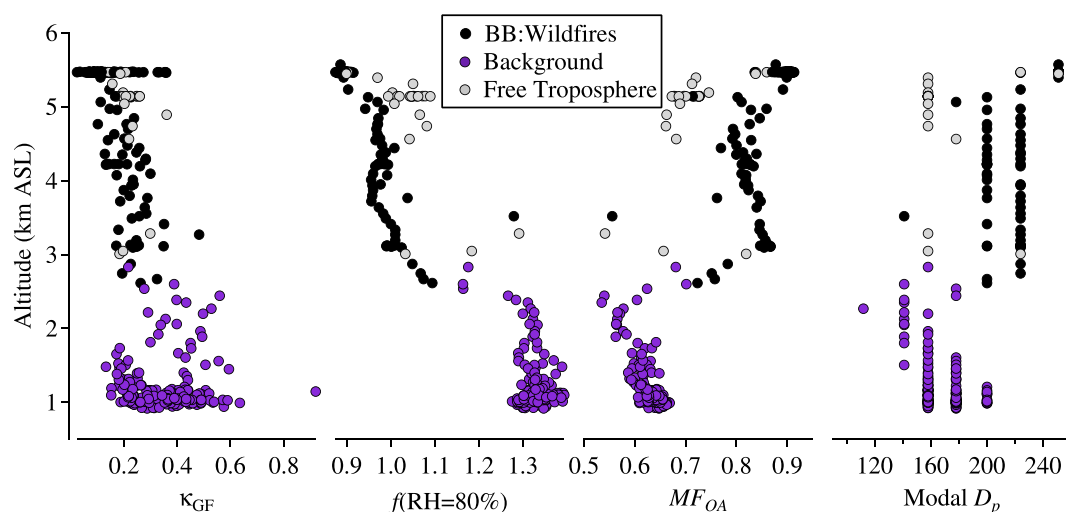
Figure 15. Vertical profiles of DASH-SP κ_{GF}, LARGE f(RH = 80%), MF$_{OA}$, and modal D_p. Data shown are from 19 August 2013 between approximately 15:10 and 16:45 local time. Markers are colored with air mass classification.

from Wyoming (Figure 14). The aged smoke was in a plume approximately 1 km thick, at an elevation of approximately 5.5 km asl, as identified by the sharp increase in aerosol backscatter (at 532 nm) from the HSRL instrument (Figure 14b). The aircraft descended from the FT into the PBL through the plume and subsequently started the first leg of a so-called "wall pattern." This pattern consisted of three legs within the same vertical plane, along a 50°/230° heading, with a length of approximately 170 km, extending from southern Kansas into the Oklahoma Panhandle. The first leg of the wall pattern was at a constant altitude of approximately 1 km asl. The second leg returned along the reverse heading, climbing from 1 km to approximately 5.5 km asl, entering the smoke plume. The third and final leg returned along the original heading of the first leg at a level altitude of approximately 5.5 km asl, until completing the length of the wall before changing heading to return to the airfield.

PBL measurements along the first leg revealed relatively homogeneous composition across the length of the leg (MF: ~0.25 sulfate, ~0.15 ammonium, and ~0.60 organic) with high hygroscopic growth, having an average κ_{GF} value of 0.36 (sampled at $D_{p,dry}$~195 nm, ~80% RH). Peak submicron aerosol mass concentrations (48.3 µg m^{-3}) were measured upon entering the smoke plume at the end of the second leg (labeled "L4" in Figure 14), corresponding with an increase in MF$_{OA}$ to greater than 0.90, and κ_{GF} values less than 0.10 (sampled at $D_{p,dry}$~300 nm, ~90% RH). Upon completing the final leg and starting to exit the plume, mass concentrations decreased and nitrate mass fractions significantly increased up to a maximum of 0.13, coinciding with a κ_{GF} value of ~0.2.

Vertical profiles of hygroscopicity, MF$_{OA}$, and LAS modal D_p are displayed in Figure 15. Hygroscopicity decreases with increasing altitude, based on both κ_{GF} and f(RH = 80%) values. Interestingly, κ_{GF} accounts for a wider range of values at all altitudes versus f(RH = 80%), especially in the background air mass type at low altitudes. This is most likely due to the DASH-SP scanning $D_{p,dry}$ values between 180 and 305 nm, as already highlighted in Figure 9. κ_{GF}, and to a larger extent f(RH = 80%), expectedly exhibit opposite trends with MF$_{OA}$ as a function of altitude. The modal D_p increases as a function of altitude as sampling extends from the boundary layer up into the smoke layer aloft, which is consistent with earlier results of higher modal D_p values coincident with higher MF$_{OA}$ and reduced κ_{GF} during SEAC^{4}RS owing to these conditions being associated with biomass burning.

5. Conclusions

This study reports on an unprecedented set of airborne RI$_{dry}$ and subsaturated aerosol hygroscopicity data from the surface up to over 6 km in altitude during the 2013 summertime SEAC^{4}RS campaign. The focus of this work is on data obtained from the DASH-SP. The main results are as follows:

1. Thermokinetic simulations were conducted to estimate the upper limit impact of volatilization within the DASH-SP during SEAC^{4}RS, with the results being applicable to other aerosol instruments with similar

residence time and dilution conditions. The volatility of SVOCs is more sensitive to a change in temperature difference (i.e., instrument-ambient) than a change in sampling RH. Furthermore, losses are greatly reduced with a semisolid particle phase state rather than with a liquid phase owing to the reduction in the bulk diffusivity of water and organics in the former case.

2. The SEAC^{4}RS data set covering numerous air types shows that an assumption of a RI$_{dry}$ (at 532 nm) within the narrow range of 1.52–1.54 is suitable based on DASH-SP measurements. When examining the hygroscopicity data, it is clear that marine and BB air mass types should be treated differently in terms of model parameterization values as compared to the blend of other air mass types encountered (biogenic, urban, background in PBL, and FT) that have intermediate properties.

3. Vertical profile data reveal that κ_{GF} exhibits minor variations with altitude (0.04–0.10 from surface to ~6.5 km) except for marine (increase) and FT (decrease) categories, which is explained by reductions (enhancements) in MF$_{OA}$ with altitude, respectively. RI$_{dry}$ values also exhibited minor variations with altitude for most air categories with the greatest ranges being for the biogenic (1.50–1.54) and marine categories (1.50–1.53), with decrease as a function of altitude for both.

4. The growth of particles measured by the DASH-SP is underestimated by the predicted value derived from the bulk f(RH) measurement for all air mass types due most likely to particles outside the DASH-SP size range being less hygroscopic.

5. κ_{GF} and f(RH = 80%) are inversely related to MF$_{OA}$. $\kappa_{GF,OA}$ and $\kappa_{GF,IOA}$ values were derived from all SEAC^{4}RS data and shown to be 0.07 and 0.50, respectively. Analogous values for f(RH = 80%)$_{OA}$ and f(RH = 80%)$_{IOA}$ were 0.92 and 2.19, respectively. $\kappa_{GF,OA}$ increases (0.06 to 0.13) as a function of the O:C ratio between 0.4 and 1.0.

6. Comparisons between the two urban centers studied, Los Angeles and Houston, show how the higher MF$_{OA}$ values in the former resulted in lower overall aerosol hygroscopicity. During the Los Angeles case study, enhanced κ_{GF} values were observed east of the Los Angeles Basin in the warmer outflow region (0.15–0.35) as compared to inside the Basin (~0.07), which exhibited higher MF$_{OA}$ and lower O:C ratios. Aerosol downwind of the Houston Downtown region exhibited higher MF$_{OA}$ as compared to the Ship Channel, resulting in lower hygroscopic growth (κ_{GF}~0.21 versus ~0.37, respectively).

7. A case study in the Kansas-Oklahoma area shows how hygroscopicity can change drastically with altitude due to biomass burning plumes. In this particular flight where BB plumes were intercepted aloft, there was suppressed aerosol hygroscopicity, size distributions shifted to larger sizes, and the composition shifted to higher MF$_{OA}$ and reduced O:C ratio values.

These results build a useful archive of size-resolved subsaturated hygroscopicity and RI$_{dry}$ across North America up to unprecedented altitudes with a fast time response instrument. Subsequent work with this data set aims to focus on the following: (i) the degree of agreement in water-uptake properties across a range of RHs extending into the super saturated regime, which is useful to determine how valid single parameters such as κ are for use in models; (ii) the ability of simple mixing rules to predict measured RI$_{dry}$ and hygroscopic GFs; and (iii) investigating the source of sub-1.0 GFs and multimodal RI$_{dry}$ distributions (dry mixing state).

References

ASDC (2015), SEAC4RS, NASA Airborne Sci. Data for Atmos. Compos., doi: 10.5067/Aircraft/SEAC4RS/Aerosol-TraceGas-Cloud. [Available at http://www-air.larc.nasa.gov/missions/seac4rs/.]

Betancourt, R. M., and A. Nenes (2014), Understanding the contributions of aerosol properties and parameterization discrepancies to droplet number variability in a global climate model, *Atmos. Chem. Phys.*, 14, 4809–4826, doi:10.5194/acp-14-4809-2014.

Brock, C. A., et al. (2015), Aerosol optical properties in the southeastern United States in summer – part 1: Hygroscopic growth, *Atmos. Chem. Phys. Discuss.*, 15, 25,695–25,738, doi:10.5194/acpd-15-25695-2015.

Canagaratna, M. R., et al. (2007), Chemical and microphysical characterization of ambient aerosols with the aerodyne aerosol mass spectrometer, *Mass Spectrom. Rev.*, 26(2), 185–222, doi:10.1002/mas.20115.

Canagaratna, M. R., et al. (2015), Elemental ratio measurements of organic compounds using aerosol mass spectrometry: Characterization, improved calibration, and implications, *Atmos. Chem. Phys.*, 15(1), 253–272, doi:10.5194/acp-15-253-2015.

Cappa, C. D., D. L. Che, S. H. Kessler, J. H. Kroll, and K. R. Wilson (2011), Variations in organic aerosol optical and hygroscopic properties upon heterogeneous OH oxidation, *J. Geophys. Res.*, 116, D15204, doi:10.1029/2011JD015918.

Carrico, C. M., M. J. Rood, and J. A. Ogren (1998), Aerosol light scattering properties at Cape Grim, Tasmania, during the First Aerosol Characterization Experiment (ACE 1), *J. Geophys. Res.*, 103, 16,565–16,574, doi:10.1029/98JD00685.

Carrico, C. M., M. J. Rood, J. A. Ogren, C. Neususs, A. Wiedensohler, and J. Heintzenberg (2000), Aerosol optical properties at Sagres, Portugal during ACE-2, *Tellus, Ser. B*, 52(2), 694–715, doi:10.1034/j.1600-0889.2000.00049.x.

Carrico, C. M., P. Kus, M. J. Rood, P. K. Quinn, and T. S. Bates (2003), Mixtures of pollution, dust, sea salt, and volcanic aerosol during ACE-Asia: Radiative properties as a function of relative humidity, *J. Geophys. Res.*, 108(D23), 8650, doi:10.1029/2003JD003405.

Chin, M., P. Ginoux, S. Kinne, O. Torres, B. N. Holben, B. N. Duncan, R. V. Martin, J. A. Logan, A. Higurashi, and T. Nakajima (2002), Tropospheric aerosol optical thickness from the GOCART model and comparisons with satellite and Sun photometer measurements, *J. Atmos. Sci.*, *59*(3), 461–483, doi:10.1175/1520-0469(2002)059<0461:Taotft>2.0.Co;2.

Coggon, M. M., A. Sorooshian, Z. Wang, J. S. Craven, A. R. Metcalf, J. J. Lin, A. Nenes, H. H. Jonsson, R. C. Flagan, and J. H. Seinfeld (2014), Observations of continental biogenic impacts on marine aerosol and clouds off the coast of California, *J. Geophys. Res. Atmos.*, *119*, 6724–6748, doi:10.1002/2013JD021228.

Compernolle, S., K. Ceulemans, and J. F. Muller (2011), EVAPORATION: A new vapour pressure estimation method for organic molecules including non-additivity and intramolecular interactions, *Atmos. Chem. Phys.*, *11*(18), 9431–9450, doi:10.5194/acp-11-9431-2011.

Corr, C. A., S. R. Hall, K. Ullmann, B. E. Anderson, A. J. Beyersdorf, K. L. Thornhill, M. J. Cubison, J. L. Jimenez, A. Wisthaler, and J. E. Dibb (2012), Spectral absorption of biomass burning aerosol determined from retrieved single scattering albedo during ARCTAS, *Atmos. Chem. Phys.*, *12*(21), 10,505–10,518.

DeCarlo, P. F., et al. (2006), Field-deployable, high-resolution, time-of-flight aerosol mass spectrometer, *Anal. Chem.*, *78*(24), 8281–8289, doi:10.1021/ac061249n.

de Gouw, J., and C. Warneke (2007), Measurements of volatile organic compounds in the Earth's atmosphere using proton-transfer-reaction mass spectrometry, *Mass Spectrom. Rev.*, *26*(2), 223–257, doi:10.1002/mas.20119.

de Gouw, J. A., et al. (2004), Chemical composition of air masses transported from Asia to the U. S. West Coast during ITCT 2K2: Fossil fuel combustion versus biomass-burning signatures, *J. Geophys. Res.*, *109*, D23S20, doi:10.1029/2003JD004202.

Dick, W. D., P. Saxena, and P. H. McMurry (2000), Estimation of water uptake by organic compounds in submicron aerosols measured during the Southeastern Aerosol and Visibility Study, *J. Geophys. Res.*, *105*, 1471–1479, doi:10.1029/1999JD901001.

Diskin, G. S., J. R. Podolske, G. W. Sachse, and T. A. Slate (2002), Open-path airborne tunable diode laser hygrometer, in *Diode Lasers and Applications in Atmospheric Sensing*, vol. 4817, edited by A. Fried, pp. 196–204, Seattle, Wash., doi:10.1117/12.453736.

Dubovik, O., and M. D. King (2000), A flexible inversion algorithm for retrieval of aerosol optical properties from Sun and sky radiance measurements, *J. Geophys. Res.*, *15*, 20,673–20,696, doi:10.1029/2000JD900282.

Dubovik, O., A. Smirnov, B. N. Holben, M. D. King, Y. J. Kaufman, T. F. Eck, and I. Slutsker (2000), Accuracy assessments of aerosol optical properties retrieved from Aerosol Robotic Network (AERONET) Sun and sky radiance measurements, *J. Geophys. Res.*, *105*, 9791–9806, doi:10.1029/2000JD900040.

Dubovik, O., B. Holben, T. F. Eck, A. Smirnov, Y. J. Kaufman, M. D. King, D. Tanre, and I. Slutsker (2002), Variability of absorption and optical properties of key aerosol types observed in worldwide locations, *J. Atmos. Sci.*, *59*(3), 590–608.

Duong, H. T., A. Sorooshian, J. S. Craven, S. P. Hersey, A. R. Metcalf, X. L. Zhang, R. J. Weber, H. Jonsson, R. C. Flagan, and J. H. Seinfeld (2011), Water-soluble organic aerosol in the Los Angeles Basin and outflow regions: Airborne and ground measurements during the 2010 CalNex field campaign, *J. Geophys. Res.*, *116*, D00V04, doi:10.1029/2011JD016674.

Duplissy, J., et al. (2011), Relating hygroscopicity and composition of organic aerosol particulate matter, *Atmos. Chem. Phys.*, *11*(3), 1155–1165, doi:10.5194/acp-11-1155-2011.

Ferrare, R. A., S. H. Melfi, D. N. Whiteman, K. D. Evans, M. Poellot, and Y. J. Kaufman (1998), Raman lidar measurements of aerosol extinction and backscattering - 2. Derivation of aerosol real refractive index, single-scattering albedo, and humidification factor using Raman lidar and aircraft size distribution measurements, *J. Geophys. Res.*, *103*, 19,673–19,689, doi:10.1029/98JD01647.

Ferrero, L., et al. (2014), Impact of black carbon aerosol over Italian basin valleys: High-resolution measurements along vertical profiles, radiative forcing and heating rate, *Atmos. Chem. Phys.*, *14*(18), 9640–9663, doi:10.5194/acp-14-9641-2014.

Forrister, H., et al. (2015), Evolution of brown carbon in wildfire plumes, *Geophys. Res. Lett.*, *42*, 4623–4630, doi:10.1002/2015GL063897.

Gasso, S., et al. (2000), Influence of humidity on the aerosol scattering coefficient and its effect on the upwelling radiance during ACE-2, *Tellus, Ser. B*, *52*(2), 546–567, doi:10.1034/j.1600-0889.2000.00055.x.

Guyon, P., O. Boucher, B. Graham, J. Beck, O. L. Mayol-Bracero, G. C. Roberts, W. Maenhaut, P. Artaxo, and M. O. Andreae (2003), Refractive index of aerosol particles over the Amazon tropical forest during LBA-EUSTACH 1999, *J. Aerosol Sci.*, *34*(7), 883–907.

Hair, J. W., C. A. Hostetler, A. L. Cook, D. B. Harper, R. A. Ferrare, T. L. Mack, W. Welch, L. R. Izquierdo, and F. E. Hovis (2008), Airborne high spectral resolution lidar for profiling aerosol optical properties, *Appl. Opt.*, *47*(36), 6734–6752.

Hameri, K., A. Laaksonen, M. Vakeva, and T. Suni (2001), Hygroscopic growth of ultrafine sodium chloride particles, *J. Geophys. Res.*, *106*, 20,749–20,757, doi:10.1029/2000JD000200.

Hand, J. L., and S. M. Kreidenweis (2002), A new method for retrieving particle refractive index and effective density from aerosol size distribution data, *Aerosol Sci. Technol.*, *36*, 1012–1026.

Hegg, D. A., D. S. Covert, K. K. Crahan, H. H. Jonsson, and Y. Liu (2006), Measurements of aerosol size-resolved hygroscopicity at sub and supermicron sizes, *Geophys. Res. Lett.*, *33*, L21808, doi:10.1029/2006GL026747.

Hersey, S. P., A. Sorooshian, S. M. Murphy, R. C. Flagan, and J. H. Seinfeld (2009), Aerosol hygroscopicity in the marine atmosphere: A closure study using high-time-resolution, multiple-RH DASH-SP and size-resolved C-ToF-AMS data, *Atmos. Chem. Phys.*, *9*(7), 2543–2554.

Hersey, S. P., J. S. Craven, K. A. Schilling, A. R. Metcalf, A. Sorooshian, M. N. Chan, R. C. Flagan, and J. H. Seinfeld (2011), The Pasadena Aerosol Characterization Observatory (PACO): Chemical and physical analysis of the Western Los Angeles basin aerosol, *Atmos. Chem. Phys.*, *11*(15), 7417–7443, doi:10.5194/acp-11-7417-2011.

Hersey, S. P., et al. (2013), Composition and hygroscopicity of the Los Angeles Aerosol: CalNex, *J. Geophys. Res. Atmos.*, *118*, 3016–3036, doi:10.1002/jgrd.50307.

IPCC (2013), Summary for policymakers, in *Climate Change 2013: The Physical Science Basis. Contribution of Working Group I to the Fifth Assessment Report of the Intergovernmental Panel on Climate Change*, edited by T. F. Stocker et al., p. 14, Cambridge Univ. Press, Cambridge, U. K.

Jimenez, J. L., R. Bahreini, D. R. Cocker, H. Zhuang, V. Varutbangkul, R. C. Flagan, J. H. Seinfeld, C. D. O'Dowd, and T. Hoffmann (2003), New particle formation from photooxidation of diiodomethane (CH2I2), *J. Geophys. Res.*, *108*(D10), 4318, doi:10.1029/2002JD002452.

Jimenez, J. L., et al. (2009), Evolution of organic aerosols in the atmosphere, *Science*, *326*(5959), 1525–1529, doi:10.1126/science.1180353.

Kaufman, Y. J., D. Tanre, L. A. Remer, E. F. Vermote, A. Chu, and B. N. Holben (1997), Operational remote sensing of tropospheric aerosol over land from EOS moderate resolution imaging spectroradiometer, *J. Geophys. Res.*, *102*, 17,051–17,067, doi:10.1029/96JD03988.

Kaufman, Y. J., I. Koren, L. A. Remer, D. Rosenfeld, and Y. Rudich (2005), The effect of smoke, dust, and pollution aerosol on shallow cloud development over the Atlantic Ocean, *Proc. Natl. Acad. Sci. U.S.A.*, *102*(32), 11,207–11,212, doi:10.1073/pnas.0505191102.

Kim, H., and S. E. Paulson (2013), Real refractive indices and volatility of secondary organic aerosol generated from photooxidation and ozonolysis of limonene, -pinene and toluene, *Atmos. Chem. Phys.*, *13*, 7711–7723, doi:10.5194/acp-13-7711-2013.

Kim, J., S. C. Yoon, A. Jefferson, and S. W. Kim (2006), Aerosol hygroscopic properties during Asian dust, pollution, and biomass burning episodes at Gosan, Korea in April 2001, *Atmos. Environ.*, *40*(8), 1550–1560, doi:10.1016/j.atmosenv.2005.10.044.

Koepke, P., M. Hess, I. Schult, and E. P. Shettle (1997), Global aerosol dataset, *Rep. 243*, 44 pp., Max-Plank-Inst. für Meteorol., Hamburg.

Kotchenruther, R. A., and P. V. Hobbs (1998), Humidification factors of aerosols from biomass burning in Brazil, *J. Geophys. Res.*, *103*, 32,081–32,089, doi:10.1029/98JD00340.

Kreidenweis, S. M., and A. Asa-Awuku (2014), Aerosol hygroscopicity: Particle water content and its role in atmospheric processes, in *Treatise on Geochemistry*, 2nd ed., edited by H. D. H. K. Turekian, chap. 5.13, pp. 331–361, Elsevier, Oxford, doi:10.1016/B978-0-08-095975-7.00418-6.

Levin, Z., and W. R. Cotton (2009), *Aerosol Pollution Impact on Precipitation: A Scientific Review*, xxi, 386 pp., Springer, London.

Li, H. H. (1976), Refractive index of alkali halides and its wavelength and temperature derivatives, *J. Phys. Chem. Ref. Data*, *5*, 329.

Liu, B. Y. H., D. Y. H. Pui, K. T. Whitby, D. B. Kittelson, Y. Kousaka, and R. L. Mckenzie (1978), Aerosol mobility chromatograph - new detector for sulfuric-acid aerosols, *Atmos. Environ.*, *12*(1–3), 99–104, doi:10.1016/0004-6981(78)90192-0.

Lohmann, U., and J. Feichter (2005), Global indirect aerosol effects: A review, *Atmos. Chem. Phys.*, *5*, 715–737.

Massoli, P., et al. (2010), Relationship between aerosol oxidation level and hygroscopic properties of laboratory generated secondary organic aerosol (SOA) particles, *Geophys. Res. Lett.*, *37*, L24801, doi:10.1029/2010GL045258.

Maudlin, L. C., Z. Wang, H. H. Jonsson, and A. Sorooshian (2015), Impact of wildfires on size-resolved aerosol composition at a coastal California site, *Atmos. Environ.*, *119*, 59–68, doi:10.1016/j.atmosenv.2015.08.039.

McInnes, L., M. Bergin, J. Ogren, and S. Schwartz (1998), Apportionment of light scattering and hygroscopic growth to aerosol composition, *Geophys. Res. Lett.*, *25*, 513–516, doi:10.1029/98GL00127.

McNaughton, C. S., et al. (2007), Results from the DC-8 Inlet Characterization Experiment (DICE): Airborne versus surface sampling of mineral dust and sea salt aerosols, *Aerosol Sci. Technol.*, *41*(2), 136–159, doi:10.1080/02786820601118406.

Metcalf, A. R., J. S. Craven, J. J. Ensberg, J. Brioude, W. Angevine, A. Sorooshian, H. T. Duong, H. H. Jonsson, R. C. Flagan, and J. H. Seinfeld (2012), Black carbon aerosol over the Los Angeles Basin during CalNex, *J. Geophys. Res.*, *117*, D00V13, doi:10.1029/2011JD017255.

Meyer, N. K., et al. (2009), Analysis of the hygroscopic and volatile properties of ammonium sulphate seeded and unseeded SOA particles, *Atmos. Chem. Phys.*, *9*(2), 721–732.

Murphy, S. M., et al. (2009), Comprehensive simultaneous shipboard and airborne characterization of exhaust from a modern container ship at sea, *Environ. Sci. Technol.*, *43*(13), 4626–4640.

Myhre, G., F. Stordal, M. Johnsrud, Y. J. Kaufman, D. Rosenfeld, T. Storelvmo, J. E. Kristjansson, T. K. Berntsen, A. Myhre, and I. S. A. Isaksen (2007), Aerosol-cloud interaction inferred from MODIS satellite data and global aerosol models, *Atmos. Chem. Phys.*, *7*(12), 3081–3101.

Petters, M. D., and S. M. Kreidenweis (2007), A single parameter representation of hygroscopic growth and cloud condensation nucleus activity, *Atmos. Chem. Phys.*, *7*(8), 1961–1971.

Rader, D. J., and P. H. McMurry (1986), Application of the tandem differential mobility analyzer to studies of droplet growth or evaporation, *J. Aerosol Sci.*, *17*(5), 771–787, doi:10.1016/0021-8502(86)90031-5.

Raut, J. C., and P. Chazette (2008), Vertical profiles of urban aerosol complex refractive index in the frame of ESQUIF airborne measurements, *Atmos. Chem. Phys.*, *8*, 901–919.

Redemann, J., et al. (2000), Retrieving the vertical structure of the effective aerosol complex index of refraction from a combination of aerosol in situ and remote sensing measurements during TARFOX, *J. Geophys. Res.*, *105*, 9949–9970, doi:10.1029/1999JD901044.

Reid, J. S., R. Koppmann, T. F. Eck, and D. P. Eleuterio (2005), A review of biomass burning emissions part II: Intensive physical properties of biomass burning particles, *Atmos. Chem. Phys.*, *5*, 799–825.

Rickards, A. M. J., R. E. H. Miles, J. F. Davies, F. H. Marshall, and J. P. Reid (2013), Measurements of the sensitivity of aerosol hygroscopicity and the kappa parameter to the O/C ratio, *J. Phys. Chem. A*, *117*(51), 14,120–14,131.

Rosati, B., et al. (2015), Vertical profiling of aerosol hygroscopic properties in the planetary boundary layer during the PEGASOS campaigns, *Atmos. Chem. Phys. Discuss.*, *15*, 9445–9505.

Sachse, G. W., G. F. Hill, L. O. Wade, and M. G. Perry (1987), Fast-response, high-precision carbon-monoxide sensor using a tunable diode-laser absorption technique, *J. Geophys. Res.*, *92*, 2071–2081, doi:10.1029/JD092id02p02071.

Schwarz, J. P., A. E. Perring, M. Z. Markovic, R. S. Gao, S. Ohata, J. Langridge, D. Law, R. McLaughlin, and D. W. Fahey (2015), Technique and theoretical approach for quantifying the hygroscopicity of black-carbon-containing aerosol using a single particle soot photometer, *J. Aerosol Sci.*, *81*, 110–126, doi:10.1016/j.jaerosci.2014.11.009.

Sheridan, P. J., D. J. Delene, and J. A. Ogren (2001), Four years of continuous surface aerosol measurements from the Department of Energy's Atmospheric Radiation Measurement Program Southern Great Plains Cloud and Radiation Testbed site, *J. Geophys. Res.*, *106*, 20,735–20,747, doi:10.1029/2001JD000785.

Shiraiwa, M., M. Ammann, T. Koop, and U. Poschl (2011), Gas uptake and chemical aging of semisolid organic aerosol particles, *Proc. Natl. Acad. Sci. U.S.A.*, *108*(27), 11,003–11,008, doi:10.1073/pnas.1103045108.

Shiraiwa, M., C. Pfrang, T. Koop, and U. Poschl (2012), Kinetic multi-layer model of gas-particle interactions in aerosols and clouds (KM-GAP): Linking condensation, evaporation and chemical reactions of organics, oxidants and water, *Atmos. Chem. Phys.*, *12*(5), 2777–2794, doi:10.5194/acp-12-2777-2012.

Shiraiwa, M., A. Zuend, A. K. Bertram, and J. H. Seinfeld (2013), Gas-particle partitioning of atmospheric aerosols: Interplay of physical state, non-ideal mixing and morphology, *Phys. Chem. Chem. Phys.*, *15*(27), 11,441–11,453, doi:10.1039/c3cp51595h.

Sjogren, S., M. Gysel, E. Weingartner, U. Baltensperger, M. J. Cubison, H. Coe, A. A. Zardini, C. Marcolli, U. K. Krieger, and T. Peter (2007), Hygroscopic growth and water uptake kinetics of two-phase aerosol particles consisting of ammonium sulfate, adipic and humic acid mixtures, *J. Aerosol Sci.*, *38*(2), 157–171, doi:10.1016/j.jaerosci.2006.11.005.

Sokolik, I. N., and O. B. Toon (1999), Incorporation of mineralogical composition into models of the radiative properties of mineral aerosol from UV to IR wavelengths, *J. Geophys. Res.*, *104*, 9423–9444, doi:10.1029/1998JD200048.

Sorooshian, A., S. Hersey, F. J. Brechtel, A. Corless, R. C. Flagan, and J. H. Seinfeld (2008a), Rapid, size-resolved aerosol hygroscopic growth measurements: Differential aerosol sizing and hygroscopicity spectrometer probe (DASH-SP), *Aerosol Sci. Technol.*, *42*(6), 445–464, doi:10.1080/02786820802178506.

Sorooshian, A., S. N. Murphy, S. Hersey, H. Gates, L. T. Padro, A. Nenes, F. J. Brechtel, H. Jonsson, R. C. Flagan, and J. H. Seinfeld (2008b), Comprehensive airborne characterization of aerosol from a major bovine source, *Atmos. Chem. Phys.*, *8*(17), 5489–5520.

Sorooshian, A., S. M. Murphy, S. Hersey, R. Bahreini, H. Jonsson, R. C. Flagan, and J. H. Seinfeld (2010), Constraining the contribution of organic acids and AMS m/z 44 to the organic aerosol budget: On the importance of meteorology, aerosol hygroscopicity, and region, *Geophys. Res. Lett.*, *37*, L21807, doi:10.1029/2010GL044951.

Stokes, R. H., and R. A. Robinson (1966), Interactions in aqueous nonelectrolyte solutions. I. Solute-solvent equilibria, *J. Phys. Chem.*, *70*(7), 2126–2131.

Suda, S. R., M. D. Petters, A. Matsunaga, R. C. Sullivan, P. J. Ziemann, and S. M. Kreidenweis (2012), Hygroscopicity frequency distributions of secondary organic aerosols, *J. Geophys. Res.*, *117*, D04207, doi:10.1029/2011JD016823.

Swietlicki, E., et al. (2008), Hygroscopic properties of submicrometer atmospheric aerosol particles measured with H-TDMA instruments in various environments - A review, *Tellus, Ser. B*, *60*(3), 432–469, doi:10.1111/j.1600-0889.2008.00350.x.

Toon, O. B., J. B. Pollack, and B. N. Khare (1976), Optical-constants of several atmospheric aerosol species - Ammonium-sulfate, aluminum-oxide, and sodium-chloride, *J. Geophys. Res.*, *81*, 5733–5748, doi:10.1029/JC081i033p05733.

Weast, R. C. (1987), Physical constants of organic compounds, in *CRC Handbook of Chemistry and Physics*, 68th ed., edited by R. C. Weast, pp. B67–B146, CRC Press, Boca Raton, Fla.

Weber, R. J., et al. (2007), A study of secondary organic aerosol formation in the anthropogenic-influenced southeastern United States, *J. Geophys. Res.*, *112*, D13302, doi:10.1029/2007JD008408.

Weingartner, E., H. Burtscher, and U. Baltensperger (1997), Hygroscopic properties of carbon and diesel soot particles, *Atmos. Environ.*, *31*(15), 2311–2327, doi:10.1016/S1352-2310(97)00023-X.

Westphal, D. L., and O. B. Toon (1991), Simulations of microphysical, radiative, and dynamical processes in a continental-scale forest fire smoke plume, *J. Geophys. Res.*, *96*, 22,379–22,400, doi:10.1029/91JD01956.

Wex, H., M. D. Petters, C. M. Carrico, E. Hallbauer, A. Massling, G. R. McMeeking, L. Poulain, Z. Wu, S. M. Kreidenweis, and F. Stratmann (2009), Towards closing the gap between hygroscopic growth and activation for secondary organic aerosol: Part 1 - Evidence from measurements, *Atmos. Chem. Phys.*, *9*(12), 3987–3997.

Wonaschütz, A., et al. (2013), Hygroscopic properties of organic aerosol particles emitted in the marine atmosphere, *Atmos. Chem. Phys.*, *13*, 9819–9835, doi:10.5194/acp-13-9819-2013.

Wu, Z. J., et al. (2013), Relating particle hygroscopicity and CCN activity to chemical composition during the HCCT-2010 field campaign, *Atmos. Chem. Phys.*, *13*(16), 7983–7996, doi:10.5194/acp-13-7983-2013.

Yamasoe, M. A., Y. J. Kaufman, O. Dubovik, L. A. Remer, B. N. Holben, and P. Artaxo (1998), Retrieval of the real part of the refractive index of smoke particles from Sun/sky measurements during SCAR-B, *J. Geophys. Res.*, *103*, 31,893–31,902, doi:10.1029/98JD01211.

Youn, J. S., Z. Wang, A. Wonaschütz, A. Arellano, E. A. Betterton, and A. Sorooshian (2013), Evidence of aqueous secondary organic aerosol formation from biogenic emissions in the North American Sonoran Desert, *Geophys. Res. Lett.*, *40*, 3468–3472, doi:10.1002/grl.50644.

Yu, L., J. Smith, A. Laskin, C. Anastasio, J. Laskin, and Q. Zhang (2014), Chemical characterization of SOA formed from aqueous-phase reactions of phenols with the triplet excited state of carbonyl and hydroxyl radical, *Atmos. Chem. Phys.*, *14*(24), 13,801–13,816, doi:10.5194/acp-14-13801-2014.

Zelenyuk, A., Y. Cai, and D. Imre (2006), From agglomerates of spheres to irregularly shaped particles: Determination of dynamic shape factors from measurements of mobility and vacuum aerodynamic diameters, *Aerosol Sci. Technol.*, *40*(3), 197–217, doi:10.1080/02786820500529406.

Zhang, X. L., P. Massoli, P. K. Quinn, T. S. Bates, and C. D. Cappa (2014), Hygroscopic growth of submicron and supermicron aerosols in the marine boundary layer, *J. Geophys. Res. Atmos.*, *119*, 8384–8399, doi:10.1002/2013JD021213.

Zieger, P., R. Fierz-Schmidhauser, M. Gysel, J. Strom, S. Henne, K. E. Yttri, U. Baltensperger, and E. Weingartner (2010), Effects of relative humidity on aerosol light scattering in the Arctic, *Atmos. Chem. Phys.*, *10*(8), 3875–3890.

Zieger, P., et al. (2011), Comparison of ambient aerosol extinction coefficients obtained from in-situ, MAX-DOAS and LIDAR measurements at Cabauw, *Atmos. Chem. Phys.*, *11*(6), 2603–2624, doi:10.5194/acp-11-2603-2011.

Zieger, P., et al. (2012), Spatial variation of aerosol optical properties around the high-alpine site Jungfraujoch (3580 m a.s.l.), *Atmos. Chem. Phys.*, *12*(15), 7231–7249, doi:10.5194/acp-12-7231-2012.

Ziemba, L. D., et al. (2013), Airborne observations of aerosol extinction by in situ and remote-sensing techniques: Evaluation of particle hygroscopicity, *Geophys. Res. Lett.*, *40*, 417–422, doi:10.1029/2012GL054428.

Zuend, A., and J. H. Seinfeld (2013), A practical method for the calculation of liquid-liquid equilibria in multicomponent organic-water-electrolyte systems using physicochemical constraints, *Fluid Phase Equilib.*, *337*, 201–213, doi:10.1016/j.fluid.2012.09.034.

Zuend, A., C. Marcolli, B. P. Luo, and T. Peter (2008), A thermodynamic model of mixed organic-inorganic aerosols to predict activity coefficients, *Atmos. Chem. Phys.*, *8*(16), 4559–4593.

Zuend, A., C. Marcolli, T. Peter, and J. H. Seinfeld (2010), Computation of liquid-liquid equilibria and phase stabilities: Implications for RH-dependent gas/particle partitioning of organic-inorganic aerosols, *Atmos. Chem. Phys.*, *10*(16), 7795–7820, doi:10.5194/acp-10-7795-2010.

Zuend, A., C. Marcolli, A. M. Booth, D. M. Lienhard, V. Soonsin, U. K. Krieger, D. O. Topping, G. McFiggans, T. Peter, and J. H. Seinfeld (2011), New and extended parameterization of the thermodynamic model AIOMFAC: Calculation of activity coefficients for organic-inorganic mixtures containing carboxyl, hydroxyl, carbonyl, ether, ester, alkenyl, alkyl, and aromatic functional groups, *Atmos. Chem. Phys.*, *11*(17), 9155–9206.